12-2021

High Fidelity Studies in Closed-Loop Control of Unsteady Aerodynamics

Miriam Theobald-Deschine
Embry-Riddle Aeronautical University, deschinm@my.erau.edu

HIGH FIDELITY STUDIES IN CLOSED-LOOP CONTROL OF UNSTEADY AERODYNAMICS

By

Miriam Theobald-Deschine

A Thesis Submitted to the Faculty of Embry-Riddle Aeronautical University

In Partial Fulfillment of the Requirements for the Degree of

Master of Science in Aerospace Engineering

December 2021

Embry-Riddle Aeronautical University

Daytona Beach, Florida

HIGH FIDELITY STUDIES IN CLOSED-LOOP CONTROL OF UNSTEADY AERODYNAMICS

By

Miriam Theobald-Deschine

This Thesis was prepared under the direction of the candidate's Thesis Committee Chair, Dr. Vladimir Golubev, Department of Aerospace Engineering, and has been approved by the members of the Thesis Committee. It was submitted to the Office of the Senior Vice President for Academic Affairs and Provost, and was accepted in the partial fulfillment of the requirements for the Degree of Master of Science in Aerospace Engineering.

THESIS COMMITTEE

Vladimir Golubev

Chairman, Dr. Vladimir Golubev

Reda R. Mankbadi

Member, Dr. Reda Mankbadi

Member, Dr. William MacKunis

Daewon Kim Digitally signed by Daewon Kim Date: 2021.12.10 09:45:59 -05'00'

Graduate Program Coordinator, Dr. DaeWon Kim

Date

James W. Gregory Digitally signed by James W. Gregory Date: 2021.12.10 14:38:16 -05'00'

Dean of the College of Engineering, Dr. James W. Gregory

Date

Christopher Grant Digitally signed by Christopher Grant Date: 2021.12.10 16:51:51 -05'00'

Associate Provost of Academic Support, Dr. Christopher Grant

Date

ACKNOWLEDGEMENTS

"Yea, I know that I am nothing; as to my strength I am weak; therefore I will not boast of myself, but I will boast of my God, for in his strength I can do all things"

- *Alma 26:12 Book of Mormon*

I am extremely grateful to my advisor, Dr. Vladimir Golubev for his continuous support, guidance and patience. I am also grateful for my committee members Dr. William MacKunis and Dr. Reda Mankbadi for their extensive expertise and guidance. Without them, this work could not have reached its goal.

My gratitude goes towards the Gates Millennium Scholars Program, for their physical and technical contribution. Their support and funding made this work possible.

Lastly, I would like to express my gratitude to my husband, Joshua Theobald-Deschine. Without his never-ending encouragement and understanding, it would be impossible for me to complete my study.

ABSTRACT

We implement and explore the success of a nonlinear, closed loop flow control strategy based on POD-ROM focusing on boundary-layer transitional flow in high-fidelity computational studies involving FDL3DI ILES code. Controlling the boundary-layer transition from laminar to turbulent allows the laminar boundary-layer to be lengthened, decreasing skin-friction drag on an airfoil. Analyses are conducted on a flat plate with an elliptical leading edge, later to be implemented in future studies with real airfoil geometry. The feedback control design employs strategically placed synthetic-jet micro actuators and pressure sensors. The efficiency of the closed-loop flow control strategies is examined in comparison with open-loop control.

TABLE OF CONTENTS

LIST OF FIGURES

Figure Page

LIST OF TABLES

NOMENCLATURE

A_1	Forcing amplitude of PDOS1
$A_2,\ B_2,\ \bar{A}_2$	Forcing amplitudes of PDOS2
amp	Nondimensional amplitude of actuator
E	Total specific energy
$\vec{F}, \vec{G}, \vec{H}$	Inviscid vector fluxes
$\overrightarrow{F_v}, \overrightarrow{G_v}, \overrightarrow{H_v}$	Viscous vector fluxes
G	Controller Gain
g(x)	Input gain matrix
J	Jacobian of the coordinate transformation
M	Number of actuators
m	Number of snapshots
N	Number of grid points times variables considered for POD-ROM
n, r	number of POD modes
O	Observer point
p	Pressure
PDOS1	Piezoelectrically driven oscillating surface actuator 1
PDOS2	Piezoelectrically driven oscillating surface actuator 2
$\vec{Q}$	Vector of dependent variables
$\mathcal{Q}_i$	Heat flux vector
Re	Reynolds Number
S	Pressure sensor location
T	Temperature

t	Time
u, v, w	Cartesian Velocity Component
$u_{i,o}$	Controller Input/Output
$\boldsymbol{X}$	POD snapshot matrix
$x_j(t)$	POD coefficients
y	POD-ROM approximate of pressure
$\gamma_j(t)$	Actuation values, or control inputs
$\zeta_j(\xi)$	Actuation modes
ξ, η, ζ	Computational Coordinates
ρ	Density
τ	Non-dimensional time
τ_{ij}	Stress Tensor
$\phi_j(\xi)$	POD modes

ABREVIATIONS

2-D	Two-dimensional
AFRL	Airforce Research Lab
ILES	Implicit Large Eddy Simulation
POD	Proper Orthogonal Decomposition
POD-ROM	Proper Orthogonal Decomposition based Reduced Order Model
ROM	Reduced Order Model
PDOSA	Piezoelectrically Driven Oscillating Surface Actuator
TS	Tollmien-Schlichting

1. Introduction

Engineers and scientists take an important consideration of the design of modern aerospace systems to optimize aerodynamic forces such as lift and drag. Flow control has recently been a popular consideration and is constantly evolving in the field of aerodynamics. It is the practice of manipulating the flow around an object through some form of interaction to a more desired outcome. The effects of successful flow control are inclusive to lift increase, drag reduction, transitional delay of laminar to turbulent, noise suppression, and more. In this paper, closed-loop active flow control is analyzed for the purpose of delaying transition and lengthening the laminar boundary layer to reduce drag over a flat-plate using a controller design based on proper orthogonal decomposition reduced order model (POD-ROM) methods, and is compared against open-loop flow control procedures.

1.1. Drag

The effects of pressure drag, and skin friction drag over an airfoil are two drag forces frequently analyzed and help explain aerodynamic phenomena. Pressure drag is due to the massive regions of flow separation. Skin friction drag is due to shear stress acting on a surface. Figure 1.1 shows that pressure drag is dominate on the blunt bodies (the cylinders and vertical flat plate), whereas skin friction drag is dominate on the streamlined body.

Turbulent flow over a blunt body can help reduce pressure drag. This phenomenon is commonly seen over a golf ball. The dimples on a golf ball create a turbulent boundary layer on the ball, decreasing pressure drag, and allowing the ball to fly further through the air at low velocities. However, turbulent flow has the opposite effect on streamlined

bodies when skin friction drag is more prominent. The velocity gradient at the wall is steeper in turbulent boundary layers than in laminar boundary layers, thus turbulence produces larger shear stresses increasing friction drag over a surface. The velocity profiles of laminar and turbulent boundary layers are shown below in Figure 1.2.

1.2. Transitional Flow

Transition is the process of a fluid flow from laminar to turbulence. This process has been analyzed and researched for centuries. The overall picture of transition in a boundary layer over a smooth surface can be broken down into the steps (White, 2006):

1. Stable laminar flow near the leading edge.
2. Unstable two-dimensional (2-D) Tollmien-Schlichting (TS) waves.
3. Development of three-dimensional unstable waves and hairpin eddies.
4. Vortex breakdown at regions of high localized shear.
5. Cascading vortex breakdown into fully three-dimensional fluctuations.
6. Formation of turbulent spots at locally intense fluctuations.
7. Coalescence of spots into fully turbulent flow.

First, stable laminar flow at the leading edge is encountered. At a critical location x, the critical Reynolds number is defined, and transition begins to take place. Infinitesimal instabilities first appear characterized by 2-D TS waves. As these 2-D instabilities propagate downstream, they develop into 3-D instabilities then coalesce into a region where turbulent spots continually exist. Further downstream of this region, the flow reaches a fully developed turbulence state. This transition process is illustrated over a smooth flat plate in Figure 1.3. If the 2-D TS waves are mitigated upon first appearances, then the growth of these 2-D waves may be delayed.

1.3. Flow Control

Flow control is commonly categorized into passive and active flow control. Passive flow control does not require any supplemental power or control loop and is achieved through several techniques that include geometric shaping, vortex generators and placement of grooves or riblets on surfaces. In contrast, active flow control requires some type of supplemental energy. Some methods include suction or blowing and the use of synthetic jet actuators.

Active flow control can be further categorized into open-loop and closed-loop control. Open-loop control is straightforward where an actuator's output is based on a predetermined input. In the closed-loop case, actuation is guided by information from a sensor in the flow with a flow model, which is the subject of the current work. The primary objective has been the development of a control technique based on reduced-order models (ROM), namely POD-ROM.

Open-loop control has proven to be quite useful in many applications but lacks the adaptability and resilience that flight environments require. In contract, closed-loop control has the capability of meeting these requirements to deliver more desired flow outcomes under varying conditions.

1.4. Importance of Research

Many aircrafts operate in flows of moderate to high Reynolds (Re) numbers where drag may be dominated by skin friction drag. In such cases, the reduction of this friction drag can improve aircraft performances. As previously discussed, turbulent boundary layers on a surface have higher shear stresses that increase skin friction drag. Therefore,

suppressing evolving instabilities to delay transition from laminar to turbulent can increase the length of the laminar boundary layer and reduce skin friction drag.

The purpose of this research is to implement and validate closed-loop control strategies of synthetic-jet actuators against open-loop strategies that attempt to mitigate TS waves in their early development and maintain larger regions of laminar flow. This study is conducted on the benchmark problem of flat plate boundary layer transition control, with the hopes of future research development on real airfoil geometry.

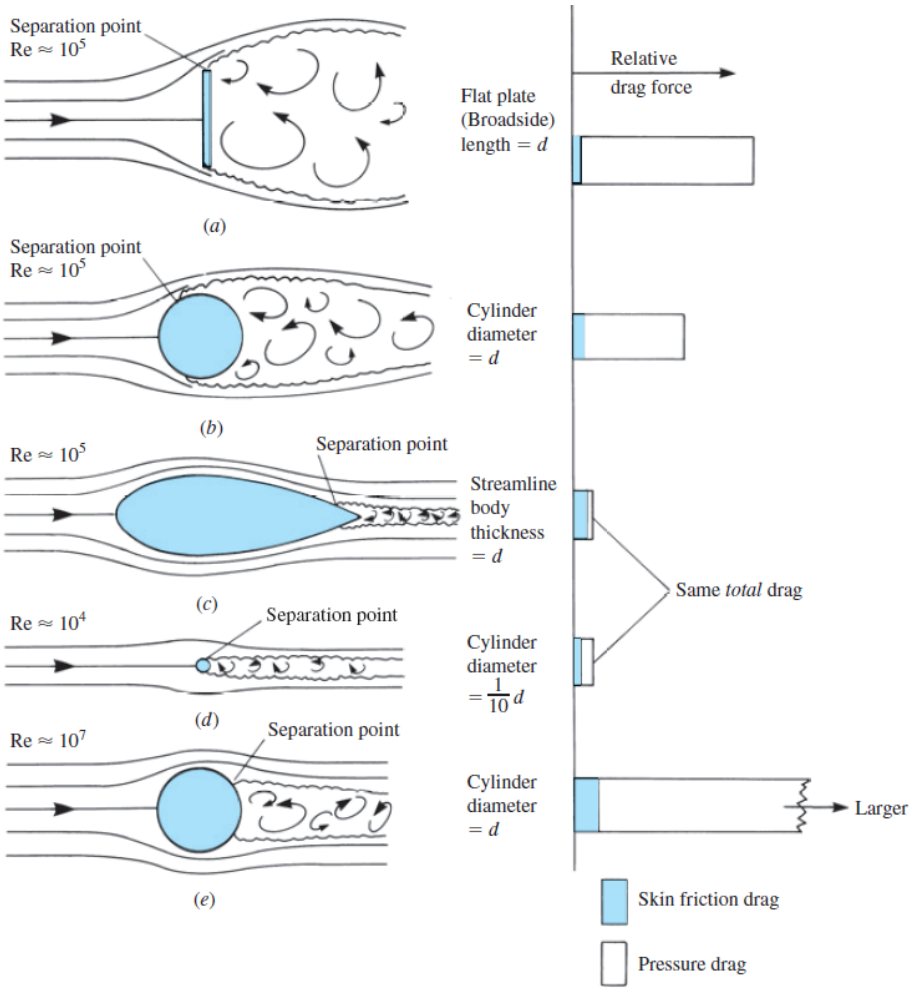

Figure 1.1 A comparison between skin friction drag and pressure drag for various aerodynamic shapes (Anderson, 2017).

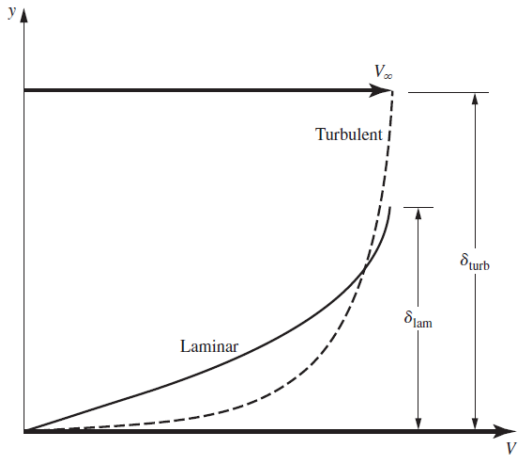

Figure 1.2 Laminar and Turbulent boundary layers (Anderson, 2017).

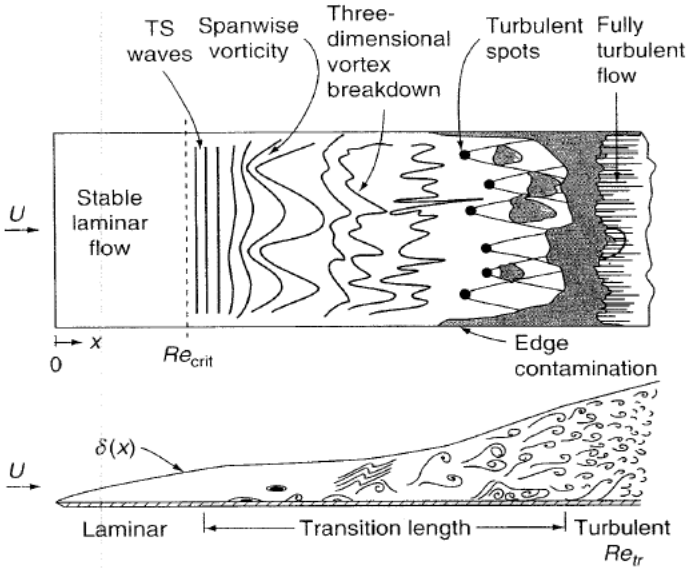

Figure 1.3 Cartoon of transition to turbulence in a boundary layer in which the plate is flat and smooth and the level of free-stream turbulence is low (White, 2006).

2. Review of the Relevant Literature

This section covers relevant literature to this research study. The first section discusses Amitay et al. (2016), and Rizzetta and Visbal (2019 & 2020), who have conducted experimental and computational studies on a flat plate. The computational studies by Rizzetta and Visbal (2019 &2020) were influenced by and closely follow the experiment of Amitay et al. (2016). The current study closely follows the computational set up of Rizzetta and Visbal (2020). The second section discusses literature that implements POD-ROM closed-loop control procedures.

2.1. Flat Plate Studies

Research on transition control to better understand it and improve modern technology has been ongoing for years. One specific study done by Rizzetta and Visbal was conducted on a flat plate with an elliptical leading edge. In Rizzetta and Visbal (2019) a computational fluid dynamics (CFD) simulation was conducted and compared against the experiment of Amitay et al. (2016). The experiment of Amitay et al. (2016) enacts control of TS waves using linear superposition of waves. Thus, when a 2-D TS wave with a known phase and amplitude interacts with a disturbance of the same frequency and amplitude but opposite phase, the TS waves are mitigated.

Amitay et al. (2016) used two Piezoelectrically Driven Oscillating Surface (PDOS) actuators to first excite 2-D TS waves, then mitigate the instabilities with the second actuator. The schematic of the PDOS actuator is in Figure 2.1. The design consists of an oscillating rubber surface with thickness of 0.79 mm and 50A hardness, a cavity with depth of 4mm and diameter of 79.5 mm, a neck opening with diameter of 12.7 mm, and a

mounted piezoelectric disc. The moving rubber surface's diameter is limited to that of the neck opening.

A voltage is applied to the disc to create oscillations of a defined amplitude and frequency corresponding to the input. A linear stability analysis conducted by Amitay et al. (2016) provided the characteristic frequency of TS waves for this schematic to be 250 Hz. A test of the deflection of the dimple as a function of voltage for a range of frequencies surrounding 250 Hz was conducted and the results are shown in Figure 2.2.

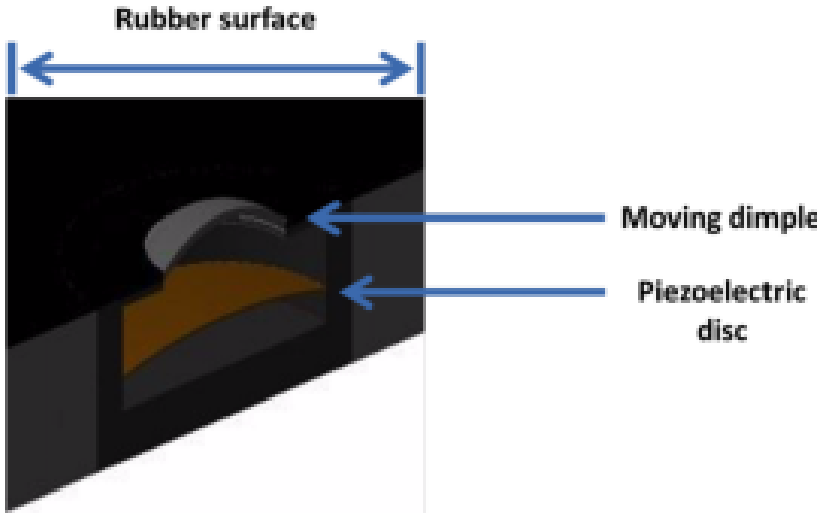

Figure 2.1 Amitay's PDOS Schematic (Amitay et al, 2016).

The experimental setup of Amitay et al (2016) is shown in Figure 2.3 and is recreated in the simulations of Rizzetta and Visbal (2019 & 2020). The flap at the trailing edge as seen in Figure 2.3 was used to adjust the location of the stagnation pressure at the leading edge and was not considered in the CFD simulations. The simulations also only consider the top half of the flat plate to reduce the computational domain. For both experimental and CFD set ups, the PDOS actuators were located at 273 mm and 388 mm from the

leading edge. Figure 2.4 shows that the location of the PDOS actuators fall in the unstable region on a boundary-layer stability curve with an oscillation frequency of 250 Hz.

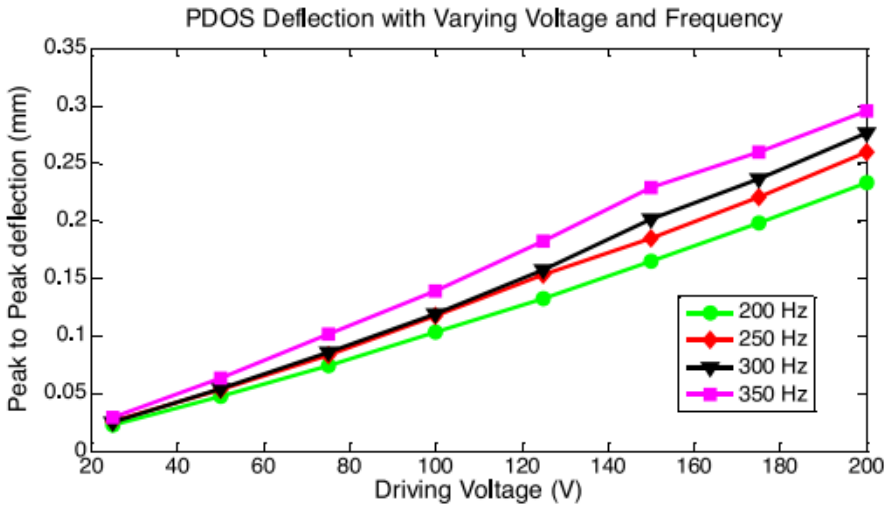

Figure 2.2 Amplitude of actuator center deflection vs input voltage (Amitay et al, 2016).

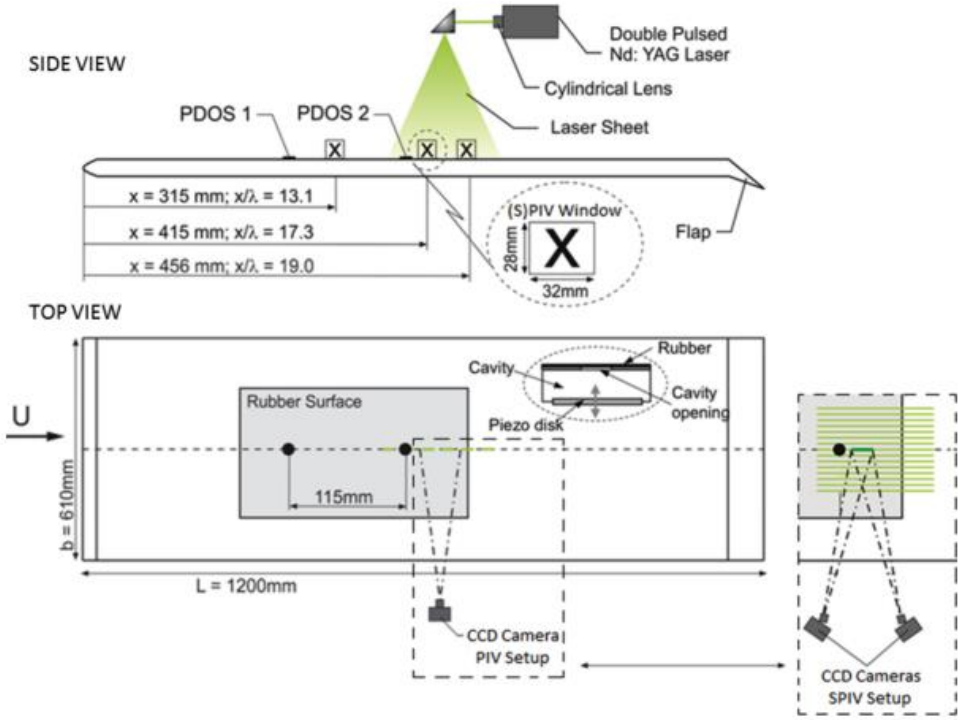

Figure 2.3 Experimental setup (Amitay, 2016).

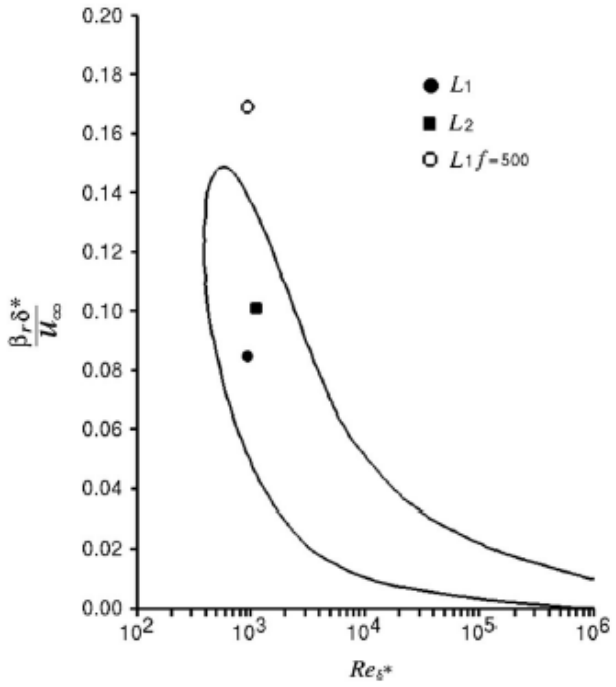

Figure 2.4 Boundary-layer stability diagram where L1=PDOS1 and L2=PDOS2 (Rizzetta & Visbal, 2019).

The role of the actuator located 273 mm from the leading edge, PDOS 1, is to introduce a disturbance to the flow to excite TS instabilities. The role of the actuator PDOS 2 located 388mm from the leading edge was to then suppress the TS waves produced by PDOS 1. Oscillations of the actuators for CFD simulations of Rizzetta and Visbal (2019 & 2020) are described by simple sine and cosine harmonic functions.

Initially, Rizzetta and Visbal's (2019) CFD configurations use the circular actuators, and the reference length of the flat plate is 500 mm. The configurations were then changed to implement spanwise actuators with lower forcing amplitudes and the reference length was increased to 1000 mm (Rizzetta & Visbal, 2020). Due to these differences, optimal amplitudes and phase shift of PDOS 2 are also different. A comparison of Rizzetta and Visbal's (2020) PDOS 2 forcing amplitudes between the 2019 and 2020 configurations can be viewed in Table 2.1. The relationship between

amplitudes A_2, B_2 and $\bar{A}_2$ is defined by a sine and cosine identity shown in Equation 2.1 below where ϕ_2 is the phase shift of PDOS 2.

$$A_2 \sin(2\pi\omega t) + B_2 \cos(2\pi\omega t) = \bar{A}_2 \sin(2\pi\omega t + \phi_2) \quad [2.1]$$

Table 2.1 PDOS Actuator 2 forcing amplitudes for 2-D configurations 1 and 2.

DESCRIPTION	**A_2**	**B_2**	**$\bar{A}_2$**	**Φ_2**
CONFIGURATION 1: 2-D	1.77E-4	8.65E-5	1.97E-4	26.04 deg
CONFIGURATION 2: 2-D	4.40E-5	1.34E-5	4.60E-5	16.94 deg

(Rizzetta & Visbal, 2020)

Rizzetta and Visbal (2020) also analyzed a closed-loop control methodology to suppress TS waves amplified by the sinusoidal input voltage applied to PDOS 1. In this closed-loop analysis, a pressure sensor is placed at 426 mm from the leading edge and is used to obtain the fluctuating component of pressure. An Iterative Learning Control (ILC) strategy is then used to modify the control input (Rizzetta & Visbal, 2020). The input for the (k+1) iteration is defined by the control law in Equation (2) and requires T in Equation (5) to first be determined. The transfer function variables γ_G and ϕ_G are estimated by system identification (Rizzetta & Visbal, 2020). The learning coefficient, ϵ, determines the convergence rate of Equation 2.5 and a value of $\epsilon = 0.5$ was used.

$$I^{k+1} = I^k - \epsilon[T^T T]^{-1} T^T P^k \quad [2.2]$$

$$I = \begin{bmatrix} \alpha_i \\ \beta_i \end{bmatrix} \quad [2.3]$$

$$P = \begin{bmatrix} \gamma_p \cos(\phi_p) \\ \gamma_p \sin(\phi_p) \end{bmatrix} \quad [2.4]$$

$$T = \begin{bmatrix} \gamma_G \cos(\phi_G) & -\gamma_G \sin(\phi_G) \\ \gamma_G \sin(\phi_G) & \gamma_G \cos(\phi_G) \end{bmatrix} \quad [2.5]$$

Finally, a visual plot of Rizzetta & Visbal's (2020) results for no control, open-loop control, and closed-loop control can be seen in Figure 2.5 below, followed by some visual results of Amitay et al. (2016). The contour plots shown in Figure 2.5 show success in suppressing 2-D TS waves on a flat plate for both open-loop and closed loop control. In a visual inspection of the results, it appears that for closed-loop control the v-velocity fluctuations are suppressed, but not as efficiently in comparison to the open-loop control.

Similarly, results of Amitay et al. (2016) in Figure 2.6 also show success of TS wave reduction. "With excitation" in Figure 2.6 corresponds to PDOS 1 active only, and "with excitation and control" corresponds to both PDOS 1 and 2 active. Figure 2.6 c, d, g, and h are plots of corresponding spectra of each velocity components indicated with a white dot as seen in Figure 2-6 a, b, e and f. The contour plots in Figure 2.6 show that instabilities existent in both streamwise and wall-normal velocities are suppressed. For more information on the results of both experimental and CFD studies refer to Amitay et al. (2016) and Rizzetta and Visbal (2020).

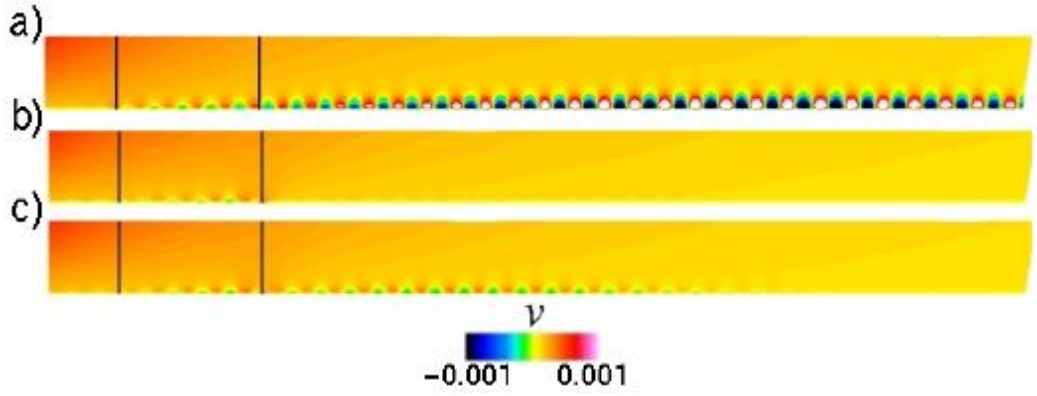

Figure 2.5 Contours of v velocity for 2-D configuration 2 simulations: a) PDOS 1 active only, b) PDOS 1 and open-loop control, c) PDOS 1 and closed loop control (Rizzetta & Visbal, 2020).

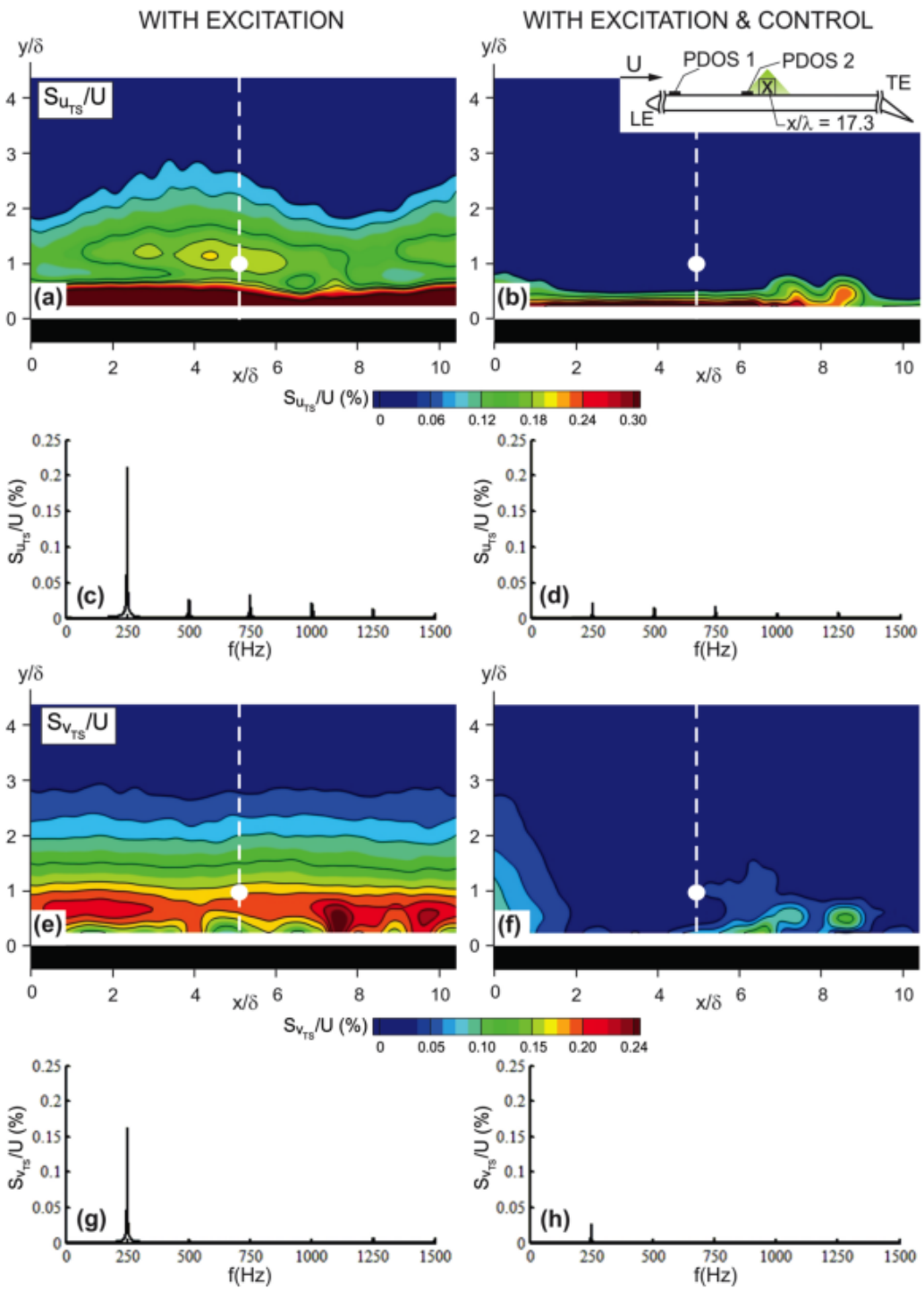

Figure 2.6 Results of experimental set up: a) and b) spectral magnitude contours of streamwise, and e) and f) wall-normal velocity with PDOS 1 active only for a) and e) and with PDOS 1 and 2 active for b) and f). Corresponding spectra of each velocity component plotted at location indicated by a white dot (Amitay et al, 2016).

2.2. Proper Orthogonal Decomposition Reduced Order Model

Modal decomposition is a mathematical technique that extracts energetically and dynamically important features of a fluid flow. Proper orthogonal decomposition (POD) is one modal analysis technique commonly used that extracts modes based on optimizing the mean square of the field variable being examined. Its objective is to decompose a set of data into a minimal number of basis modes or functions to capture as much energy as possible. One POD method under the particular interest of the current research is the method of snapshots developed by Sirovich (1987).

For a set of fluid flow data, *N* is the number of grid points times the number of variables considered, and *m* is the number of snapshots. The method of snapshots takes a collection of snapshots $\boldsymbol{X}$ of the form $\boldsymbol{X} = [x(t_1) \;\; x(t_2) \;\; ... \;\; x(t_m)]$ where $x(t_i)$, is the fluctuating component vector of size *N* (Taira et al., 2017), namely,

$$x(t) = u(\xi, t) - \bar{u}(\xi) \tag{2.6}$$

with $u(\xi, t)$ being the component vector field and $\bar{u}(\xi)$ is the mean. The POD expression to be solved is:

$$y(t) \approx u(\xi, t) - \bar{u}(\xi) \approx \sum_{j=1}^{m} x_j(t)\phi_j(\xi) \tag{2.7}$$

where $x_j(t)$ are now the coefficients and $\phi_j(\xi)$ are the POD modes. The eigenvalue problem to be solved is thus a size of ($m \times m$) and is:

$$\boldsymbol{X}^T\boldsymbol{X}\psi_j = \lambda_j\psi_j \tag{2.8}$$

If $\boldsymbol{\Phi} = [\phi_1 \;\; \phi_2 \;\; ... \;\; \phi_m]$ and $\boldsymbol{\Psi} = [\psi_1 \;\; \psi_2 \;\; ... \;\; \psi_m]$ then the POD modes are recovered by,

$$\boldsymbol{\Phi} = \boldsymbol{X}\boldsymbol{\Psi}\boldsymbol{\Lambda}^{-1/2} \tag{2.9}$$

The incompressible Navier-Stokes (NS) equations can be expressed as,

$$\nabla \cdot u = 0\,, \quad \frac{\partial u}{\partial t} = -(u \cdot \nabla)u + \nu\nabla^2(u) - \nabla p \tag{2.10}$$

where $u(\xi, t)$ is the velocity field over a spatial domain ξ; $p(\xi, t)$ is the time and space dependent pressure field and $\nu = 1/Re$. Rearranging Equations 2.6 and 2.7 into Equation 2.10 we achieve the POD-ROM of the NS equations.

$$\begin{aligned}\frac{\partial}{\partial t}\sum_{j=1}^{m} x_j(t)\phi_j(\xi) \\ = -\left(\left[\bar{u} + \sum_{j=1}^{m} x_j(t)\phi_j(\xi)\right]\cdot\nabla\right)\left[\bar{u} + \sum_{j=1}^{m} x_j(t)\phi_j(\xi)\right] \\ + \nu\nabla^2\left[\bar{u} + \sum_{j=1}^{m} x_j(t)\phi_j(\xi)\right] - \nabla p\end{aligned} \tag{2.11}$$

This set of nonlinear ordinary differential equations are not useful for controller design, and a control input needs to be expressed so that a feedback controller may be designed with control theory laws.

In Kidambi et al. (2020) the POD-ROM flow velocity field is expanded as a weighted sum of actuated and unactuated POD modes such that,

$$u(\xi, t) \approx \bar{u}(\xi) + \sum_{j=1}^{m} x_j(t)\phi_j(\xi) + \sum_{i=1}^{M} \gamma_i(t)\zeta_i(\xi) \tag{2.12}$$

where $\zeta_j(\xi)$ denotes actuation modes and $\gamma_j(t)$ denotes actuation values, or control inputs. Equation 2.12 is substituted into Equation 2.10, and the individual terms yield, (Kidambi et al., 2020),

$$\frac{\partial u}{\partial t} \approx \sum_{j=1}^{m} \dot{x}_j\phi_j + \sum_{i=1}^{M} \dot{\gamma}_i\zeta_i \tag{2.13}$$

$$\nabla^2 u \approx \nabla^2 \bar{u} + \sum_{j=1}^{m} x_j \nabla^2 \phi_j + \sum_{i=1}^{M} \gamma_i \nabla^2 \zeta_i \tag{2.14}$$

$$\begin{aligned}(u \cdot \nabla)u \approx \bar{u} \cdot \nabla \bar{u} &+ \sum_{j=1}^{m} \left(\bar{u} \cdot \nabla \phi_j + \phi_j \cdot \nabla \bar{u}\right) x_j + \sum_{i=1}^{M} (\bar{u} \cdot \nabla \zeta_i + \zeta_i \cdot \nabla \bar{u}) \gamma_i \\ &+ \sum_{j=1}^{m} \sum_{i=1}^{M} \left(\phi_j \cdot \nabla \phi_i\right) x_j x_i + \sum_{j=1}^{m} \sum_{i=1}^{M} \left(\zeta_j \cdot \nabla \zeta_i\right) \gamma_j \gamma_i \\ &+ \sum_{j=1}^{m} \sum_{i=1}^{M} \left(\phi_j \cdot \nabla \zeta_i + \zeta_i \cdot \nabla \phi_j\right) x_j \gamma_i\end{aligned} \tag{2.15}$$

By projecting Equations 2.13-2.15 onto ϕ_k, Kidambi et al. (2020) obtains Equation 2.16,

$$\begin{aligned}\dot{x_k}(t) = \mathcal{A}_k &+ \sum_{j=1}^{n} \mathcal{B}_{kj} x_j(t) + \sum_{j=1}^{n} \sum_{i=1}^{n} \mathcal{C}_{kji} x_j(t) x_i(t) + \sum_{j=1}^{n} \mathcal{D}_{kj} \dot{\gamma_j}(t) \\ &+ \sum_{j=1}^{n} \sum_{i=1}^{M} \mathcal{E}_{kji} x_j(t) \gamma_i(t) + \sum_{i=1}^{M} \mathcal{F}_{ki} \gamma_i + \sum_{i=1}^{M} \sum_{j=1}^{M} \mathcal{G}_{kij} \gamma_i(t) \gamma_j(t)\end{aligned} \tag{2.16}$$

where terms $\mathcal{A}_k$ through $\mathcal{G}_k$ are the listed in Equation 2.17.

$$\begin{aligned}\mathcal{A}_k &= -\langle \bar{u} \cdot \nabla \bar{u}, \phi_k \rangle + \frac{1}{Re} \langle \nabla^2 \bar{u}, \phi_k \rangle \\ \mathcal{B}_k &= -\langle \bar{u} \cdot \nabla \phi_j, \phi_k \rangle - \langle \phi_j \cdot \nabla \bar{u}, \phi_k \rangle + \frac{1}{Re} \langle \nabla^2 \phi_j, \phi_k \rangle \\ \mathcal{C}_k &= -\langle \phi_j \cdot \nabla \phi_i, \phi_k \rangle \\ \mathcal{D}_k &= -\langle \zeta_j, \phi_k \rangle \\ \mathcal{E}_k &= -\langle \zeta_i \cdot \nabla \phi_j, \phi_j \rangle - \langle \phi_j \cdot \nabla \zeta_i, \phi_k \rangle \\ \mathcal{F}_k &= -\langle \bar{u} \cdot \nabla \zeta_j, \phi_k \rangle - \langle \zeta_j \cdot \nabla \bar{u}, \phi_k \rangle + \frac{1}{Re} \langle \nabla^2 \zeta_j, \phi_k \rangle \\ \mathcal{G}_k &= -\langle \zeta_j \cdot \nabla \zeta_i, \phi_k \rangle\end{aligned} \tag{2.17}$$

Continuously, Kidambi et al. (2020) expressed the actuated reduced-order dynamics model Equation 2.18 in control regime,

$$\dot{x} = f(x) + g(x)u, \qquad y = h(x) \tag{2.18}$$

where x(t) contains the coefficients that result from POD-ROM, $g(x)$ is an input gain matrix and $u(t)$ is a control input and $y(t)$ is a measurable output such as flow velocity or pressure. This POD-ROM based controller by Kidambi et al. (2020) is the nonlinear closed-loop design under consideration for the current study.

3. Methodology

The project provides opportunity for future research. The long-term project goals and steps are broken down in Figure 3.1. The project analyzes two different types of closed-loop controllers and is compared against Rizzetta and Visbal (2020). For the sake of this project, an open-loop analysis was conducted and compared against Rizzetta and Visbal (2020), followed by the implementation of and analyzation of closed-loop controller 1, along with the exploration of closed-loop controller 2. Because CFD results are compared against Rizzetta and Visbal (2020), the flat plate simulation set-up is closely followed and discussed below.

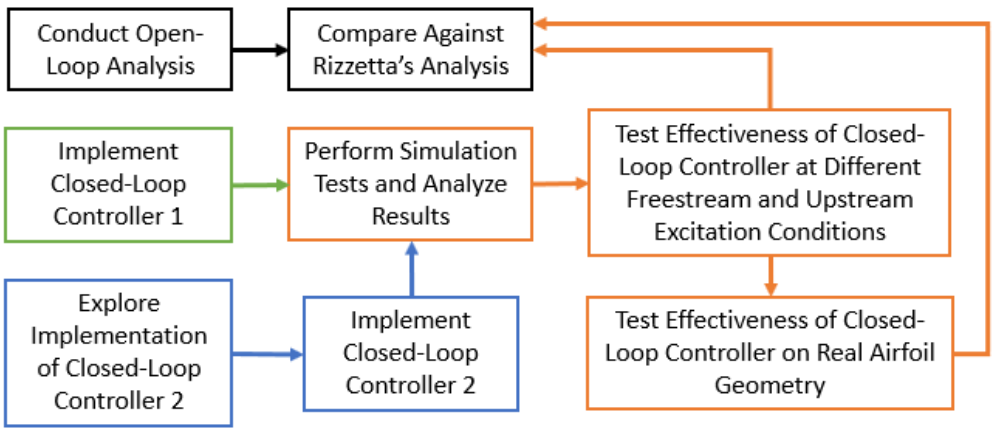

Figure 3.1 Project overview.

3.1. Problem Statement

The problem to be solved is to design a closed-loop controller that provides an input voltage to a PDOS actuator that deforms a surface in an oscillatory manner to suppress the 2-D TS waves before instabilities grow too large, lengthening the laminar boundary layer. The closed-loop analyses are first implemented on a flat plate, later to be analyzed on real airfoil geometries. The flat plate configuration is shown in Figure 3.2 and is the

same as that of configuration 2 in Rizzetta and Visbal (2020). The flat plate has a length of 1000 mm, a thickness of 19 mm, and a 4:1 elliptical leading edge. A_1 denotes the PDOS actuator 1 at L_1 = 273 mm and A_2 denotes PDOS actuator 2 at L_2 = 388 mm. Location L_3 from the leading edge denotes the location of a pressure sensor S and varies for this study. Point O is 600mm from the leading edge and is used to compare the time history of pressure for the open and closed-loop control tests.

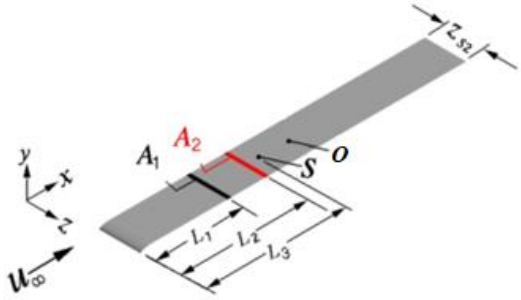

Figure 3.2 Flat Plate Configuration (Rizzetta & Visbal, 2020).

3.1.1. The Governing Equations

The governing equations solved are the unsteady, three-dimensional compressible Navier-Stokes equations in Equation 3.1. Here, t is time, ξ, η, and ζ are computational coordinates. The vectors in Equation 3.1 are defined in Equations 3.2 through 3.7.

$$\frac{\partial}{\partial t}\left(\frac{\vec{Q}}{J}\right)+\frac{\partial \vec{F_i}}{\partial \xi}+\frac{\partial \vec{G_i}}{\partial \eta}+\frac{\partial \vec{H_i}}{\partial \zeta}-\frac{1}{Re}\left[\frac{\partial \vec{F_v}}{\partial \xi}+\frac{\partial \vec{G_v}}{\partial \eta}+\frac{\partial \vec{H_v}}{\partial \zeta}\right]=\vec{S} \quad [3.1]$$

$$\vec{Q}=[\rho \quad \rho u \quad \rho v \quad \rho w \quad \rho E]^T \quad [3.2]$$

$$\vec{F}=\frac{1}{J}\begin{bmatrix}\rho U\\ \rho uU+\xi_x p\\ \rho vU+\xi_y p\\ \rho wU+\xi_z p\\ \rho EU+\xi_{x_i}u_i p\end{bmatrix} \quad \vec{G}=\frac{1}{J}\begin{bmatrix}\rho V\\ \rho uV+\eta_x p\\ \rho vV+\eta_y p\\ \rho wV+\eta_z p\\ \rho EV+\eta_{x_i}u_i p\end{bmatrix} \quad \vec{H}=\frac{1}{J}\begin{bmatrix}\rho U\\ \rho uU+\zeta_x p\\ \rho vU+\zeta_y p\\ \rho wU+\zeta_z p\\ \rho EU+\zeta_{x_i}u_i p\end{bmatrix} \quad [3.3]$$

$$\overrightarrow{F_v} = \frac{1}{J}\begin{bmatrix} 0 \\ \xi_{x_i}\tau_{i1} \\ \xi_{x_i}\tau_{i2} \\ \xi_{x_i}\tau_{i3} \\ \xi_{x_i}(u_j\tau_{ij} - Q_i) \end{bmatrix} \quad \overrightarrow{G_v} = \frac{1}{J}\begin{bmatrix} 0 \\ \eta_{x_i}\tau_{i1} \\ \eta_{x_i}\tau_{i2} \\ \eta_{x_i}\tau_{i3} \\ \eta_{x_i}(u_j\tau_{ij} - Q_i) \end{bmatrix} \quad \overrightarrow{H_v} = \frac{1}{J}\begin{bmatrix} 0 \\ \zeta_{x_i}\tau_{i1} \\ \zeta_{x_i}\tau_{i2} \\ \zeta_{x_i}\tau_{i3} \\ \zeta_{x_i}(u_j\tau_{ij} - Q_i) \end{bmatrix} \quad [3.4]$$

$$U = \xi_t + \xi_{x_i}u_i \qquad V = \eta_t + \eta_{x_i}u_i \qquad W = \zeta_t + \zeta_{x_i}u_i \quad [3.5]$$

$$E = \frac{T}{\gamma(\gamma-1)M_\infty^2} + \frac{1}{2}(u^2 + v^2 + w^2) \quad [3.6]$$

$$p = \frac{\rho T}{\gamma M_\infty^2} \quad [3.7]$$

The variables u, v, and w are Cartesian velocity components, ρ is density, p is pressure and T is temperature. Continuously, the components of the heat flux vector and stress tensor are in Equations 3.8-3.9.

$$Q_i = \left[\frac{1}{(\gamma-1)M_\infty^2}\right]\left(\frac{\mu}{Pr}\right)\frac{\delta\xi_j}{\delta x_i}\frac{T}{\delta\xi_j} \quad [3.8]$$

$$\tau_{ij} = \mu\left(\frac{\partial\xi_k}{\partial x_j}\frac{\partial u_i}{\partial\xi_k} + \frac{\partial\xi_k}{\partial x_i}\frac{\partial u_j}{\partial\xi_k} - \frac{2}{3}\delta_{ij}\frac{\partial\xi_l}{\partial x_k}\frac{\partial u_k}{\partial\xi_l}\right) \quad [3.9]$$

3.2. Computational Setup

This section encompasses the computational setup of the project, i.e., the mesh and numerical methods. The computational setup is the same as of that for Rizzetta and Visbal (2020) for comparison of results. The Airforce Research Lab (AFRL) provided

their implicit large eddy simulation (ILES) code FDL3DI for the sake of this project and its numerical methods are discussed below.

3.2.1. Computational Mesh

The computational mesh was provided by the AFRL. It is a half c-grid, consisting of the top half of the flat plate. Since the flat plate is symmetrical, only the top half is used to reduce computational expenses. The overall grid used consisted of a 4129 x 431 x 3 grid size with a total of 3,550,080 cells. The grid spacing near the wall is approximately .015 mm, resulting of a yplus less than one.

The computational grid is shown in Figure 3.3. As seen in Figure 3.3a, grid stretching can be seen in the farfield regions. This stretching helps prevent any spurious reflections in the outflow region. The 4:1 elliptical leading edge of the flat plate is shown in Figure 3.3b. In figure 3.3c, the 3-D view of the grid is shown. The grid uses 3 slices in the z-direction to be compatible with FDL3DI for a 2-D case.

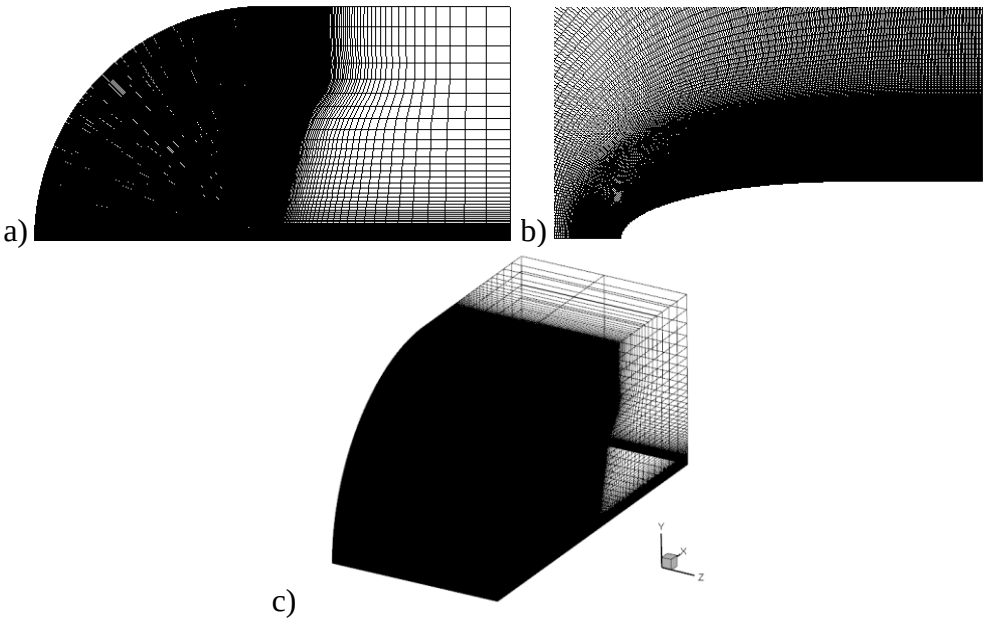

Figure 3.3 Computational Mesh, *a)* Farfield region, b) 4:1 Elliptical Leading Edge, c) 3-D view (z-direction stretched by a factor of 12).

3.2.2. AFRL FDL3DI ILES Code

The AFRL FDL3DI code is an implicit LES solver. It incorporates the sixth-order accurate Pade compact scheme for spatial derivatives and second-order backward-implicit time differencing scheme for temporal derivatives. Subiterations are utilized within a time-step to maintain temporal accuracy. In addition, to maintain stability and accuracy, a low-pass Pade-type spatial filter from Gaitonde (1997) is used with the finite differencing schemes. The filter is applied following each subiteration to the evolving solution to adjust poorly resolved features. This filtering methodology is a post-processing technique.

3.2.2.1. Freestream Conditions

Standard atmospheric conditions are assumed for this problem and are listed in Table 3.1. The Reynolds number of 1,081,642 and a Mach number of 0.1 were used to match conditions of Rizzetta and Visbal (2020). With standard atmospheric conditions, the speed of sound is 340.3 m/s, thus the velocity used is 34.03 m/s. This is slightly more than half of the freestream velocity used in the experiment of Amitay. Note that the Reynold's number calculated uses the 16 m/s of that of Amitay.

Table 3.1 Freestream Conditions.

Description	**Value**
Speed of Sound	340.3 m/s
Freestream Velocity	34.03 m/s
Pressure	1 atm.
Density	1.225 kg/m^3
Kinematic Viscosity	1.48E-5 m^2/s
Temperature	288.15 K
Ratio of Specific Heats	1.4

3.2.2.2. Boundary Condition

This section covers the boundary conditions applied to the computational domain. At the flat plate, the no-slip adiabatic wall condition is enforced. The general location of this can be seen in red in Figure 3.4. Ahead of the flat plate, an inviscid wall condition is used. The outflow boundary condition is variable extrapolation and pressure is atmospheric. The general location of this is seen in blue in Figure 3.4. Lastly, there is a freestream pressure extrapolation for the inlet as seen in green.

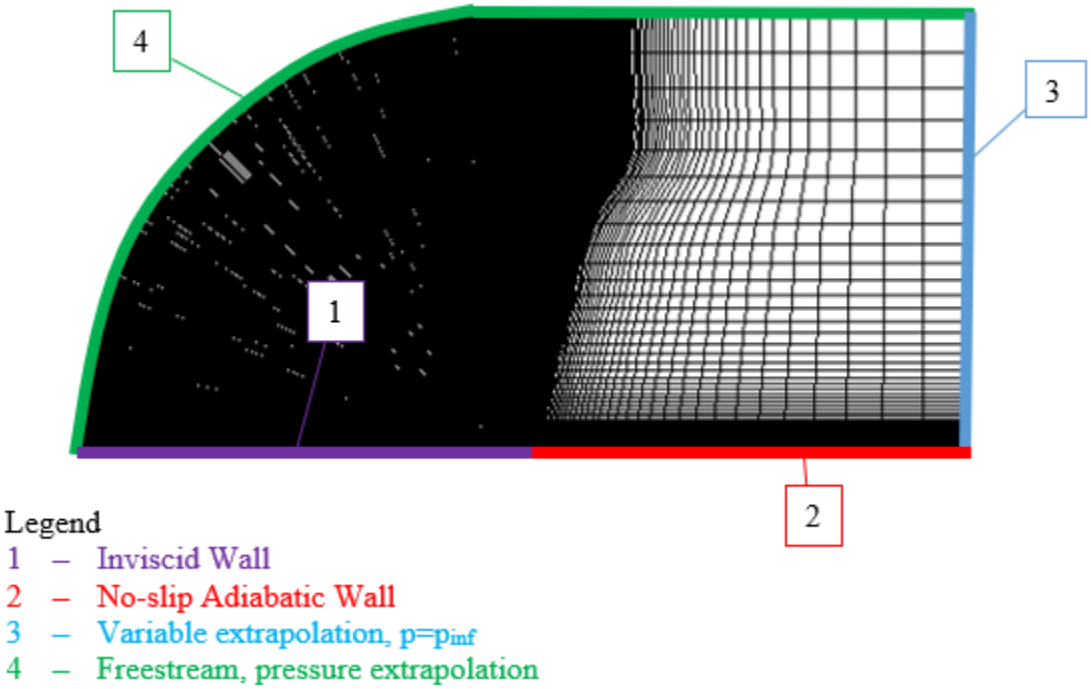

Figure 3.4 Boundary Conditions.

3.2.3. Closed-Loop Controller

The computational set-up follows that of Rizzetta and Visbal (2020), except for the closed-loop controller. This study examines two potential closed-loops controllers to

mitigate 2-D TS instabilities, Controller 1 and Controller 2. Controller 1 is a simple pressure-correction controller that uses a pressure sensor downstream of PDOS 2. Controller 2 is a non-linear controller that incorporates Proper Orthogonal Decomposition Reduced Order Model (POD-ROM) methodology.

3.2.3.1. Controller One

Controller 1 is a simple pressure-correction closed-loop controller that takes a pressure perturbation reading multiplied by a control-law gain value and outputs a voltage, u_o in Equation 3.10, read by the PDOS actuator. A black-box model of this control loop is below in Figure 3.5.

$$u_o = Gp' \quad [3.10]$$

$$p' = p_2 - \bar{p}_2 \quad [3.11]$$

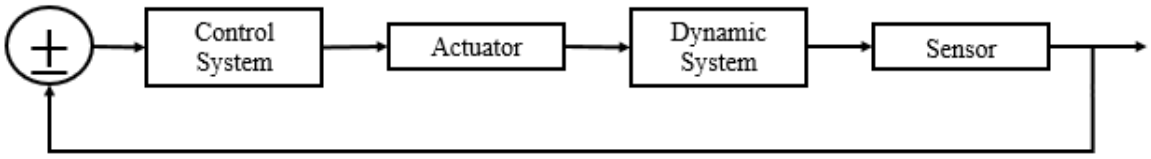

Figure 3.5 Black box model of pressure-based controller.

The pressure perturbation is calculated by the controller using Equation 3.11, where p_2 is the pressure reading from the sensor, and $\bar{p}_2$ is the averaged pressure from the sensor. This methodology allows only one sensor to be used, and no previous averaged pressure value is needed. This methodology is different than that of Rizzetta 2020, where the averaged pressure value is taken from the steady-state simulation before instabilities occur.

A downside to this methodology is suppression is delayed due to the time it takes to achieve a converged averaged pressure value. In addition, the controller gain is contingent on the location of the pressure sensor. The controller gain G in Equation 3.10 is expressed in Equation 3.12, where A_2 and B_2 are found in Table 2.1 for configuration 2. The value F is chosen arbitrarily based on the location of the pressure sensor.

$$G = \tau F^2 \sqrt{A_2^2 + B_2^2} \qquad for\ 0\ \leq \tau < 1$$
$$G = F^2 \sqrt{A_2^2 + B_2^2} \qquad for\ 1 \leq \tau \qquad [3.12]$$

3.2.3.2. Controller Two

Controller 2 is the robust nonlinear controller that incorporates POD-ROM procedures. As mentioned in Section 2.2, the controller method under consideration is that of Kidambi et al. (2020) in which Equation 2.12 is substituted into the NS equations to achieve a ROM. Kidambi et al. (2020) uses velocity as the selective component, but for the current work, a pressure sensor is used, thus the fluctuating pressure component will be under evaluation.

The black box model for this control loop is below in Figure 3.6. When comparing the black box models of the two closed-loop controller, the POD-ROM has an extra step. The POD-ROM box in Figure 3.6 represents a kind of “estimator” or “observer” that approximates flow field velocity or pressure direct measurements. In this case it is the later. The POD-ROM approximations are used as surrogates for the actual sensor measurements in the feedback control law. This is beneficial because the actual closed-loop flow control system is tested and adjusted using low-fidelity simulations that can be run within seconds or minutes, saving on computational time and expenses.

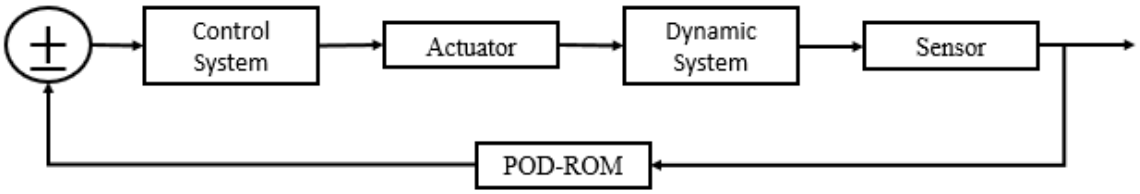

Figure 3.6 Black box model of POD-ROM based controller.

The proposed method consists of first conducting CFD simulations on the flat plate with PDOS actuator 1 active for excitation of instabilities and open loop control. Then a POD analysis is then conducted on the pressure data from the simulations. The POD analysis will provide the needed coefficient and mode data, $x_j(t)$ and $\phi_j(\xi)$ respectively, and the flow field dynamic ROM correlates to Equation 3.13.

$$\dot{x_k}(t) = \mathcal{A}_k + \sum_{j=1}^{n} \mathcal{B}_{kj} x_j(t) + \sum_{j=1}^{n}\sum_{i=1}^{n} \mathcal{C}_{kji} x_j(t) x_i(t) + \sum_{j=1}^{n} \mathcal{D}_{kj} \dot{\gamma_j}(t) + \sum_{j=1}^{n}\sum_{i=1}^{M} \mathcal{E}_{kji} x_j(t) \gamma_i(t) + \sum_{i=1}^{M} \mathcal{F}_{ki} \gamma_i + \sum_{i=1}^{M}\sum_{j=1}^{M} \mathcal{G}_{kij} \gamma_i(t) \gamma_j(t) \quad [3.13]$$

As an example, for four modes, Equation 3.13 can be expanded into the Equations 3.14-3.18, where y represents the POD-ROM approximate of pressure and u_i is the controller input.

$$\dot{x_1} = b_1 + L_{11}x_1 + Q_{141}x_1x_4 + Q_{111}x_1^2 + Q_{121}x_1x_2 + Q_{131}x_1x_3 + u_i(t) \quad [3.14]$$

$$\dot{x_2} = b_2 + [L_{22} + t_2(x_2^2 + x_3^2)]x_2 + L_{23}x_3 + Q_{121}x_1x_2 + u_i(t) \quad [3.15]$$

$$\dot{x_3} = b_3 + L_{32}x_2 + [L_{33} + t_3(x_2^2 + x_3^2)]x_3 + Q_{313}x_1x_3 + Q_{314}x_1x_4 + u_i(t) \quad [3.16]$$

$$\dot{x_4} = b_4 + L_{41}x_1 + L_{44}x_4 + Q_{444}x_4^2 + Q_{414}x_1x_4 + Q_{424}x_2x_4 + Q_{434}x_3x_4 + u_i(t) \quad [3.17]$$

$$y = c_1x_1 + c_2x_2 + c_3x_3 + c_4x_4 \quad [3.18]$$

4. Results

Three main conditions are tested and compared in this simulation environment namely: 1) Production of 2-D TS waves: Excitation without control; 2) Excitation with open-loop actuation: Open-Loop Control; and 3) Excitation with closed-loop actuation: Closed-Loop Control. The suppression of TS waves is observed through pressure and v-velocity values. Although in the real world, it should be noted that the nature of transitional flows is sensitive and thus results may change significantly between geometries. Because of this many tests and comparisons should be conducted. The simulations discussed below sheds light on the performance of the different closed-loop controllers for detecting and suppressing the growth of 2-D TS instabilities.

4.1. Excitation With No Control

The first step in simulation tests is to excite the growth of TS instabilities. This is conducted by PDOS 1 at location 273 mm from the leading edge. The streamwise wavelength of the largest amplified TS wave is obtained from linear stability theory of Amitay to be λ = 24 mm. Using a PDOS actuator of diameter half of λ produces the best control (Kotsonis, 2013)**.** A frequency of 250 Hz was used as input to the PDOS 1 to enhance disturbances. The non-dimensional amplitude of PDOS 1 can be described by Equation 4.1 where ω is 15.625.

$$amp = 2 \times 10^{-5} \times \sin(2\pi\omega\tau) \qquad [4.1]$$

The pressure and v-velocity contour plots are seen in Figure 4.1a and b respectively. The three vertical lines indicate the locations of PDOS 1 and 2 (273 mm and 388 mm from the leading edge, respectively), and an observer point O where pressure is recorded

over time. Point O is located 600mm from the leading edge. These plots visually show the existence of 2-D TS waves from excitation of PDOS 1 actuation.

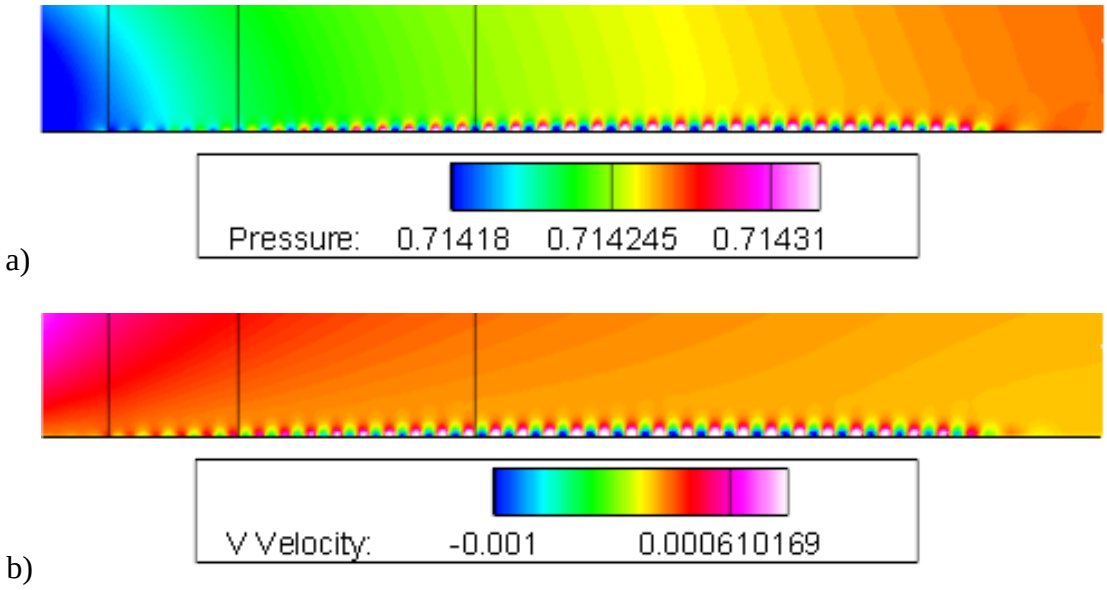

a)

b)

Figure 4.1 Excitation without control contour plots a) Pressure, b) V Velocity.

The time history plot for point O is shown below in Figure 4.2. Time at tau 0 indicates when steady-state has been reached with PDOS 1 active. It can be observed that the pressure oscillates between roughly 71.409 kPa and 71.438 kPa in Figure 4.2.

The evolution of pressure and v-velocity across the plat is also observed and is shown in Figure 4.3 and Figure 4.4 respectively. The pressure and v-velocity values are taken from 0.1m to 0.9m, for just after the elliptical leading edge and before the end of the plate. As seen in Figure 4.3, the pressure gradually increases along the plate and begins to oscillate after the first vertical line, which indicates the location of PDOS 1. The second vertical line indicates the location of PDOS 2, which is currently inactive. The third vertical line indicates the location of observer point O, the same as the contour plots. A

similar trend is seen in Figure 4.4 for v-velocity, however instead of a gradual increase upstream of PDOS 1, a gradual decrease is observed until disturbances are introduced by actuation and oscillations are observed.

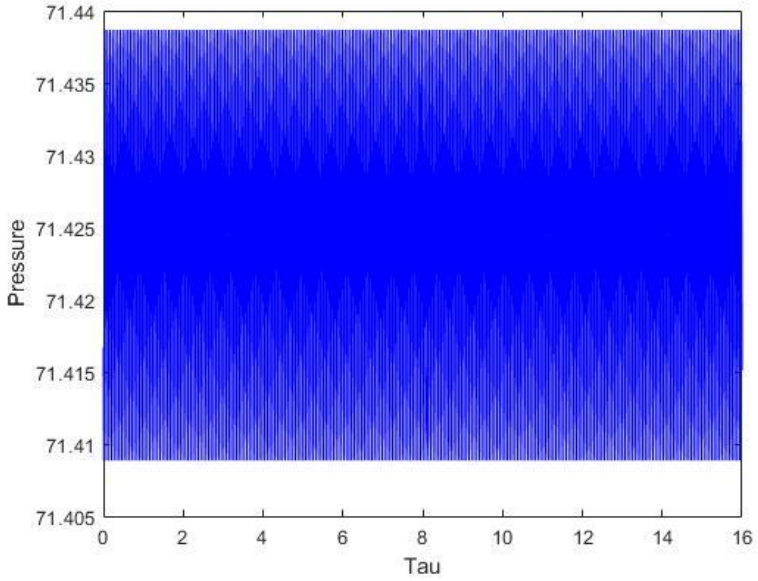

Figure 4.2 Time history plot at point O: excitation with no control.

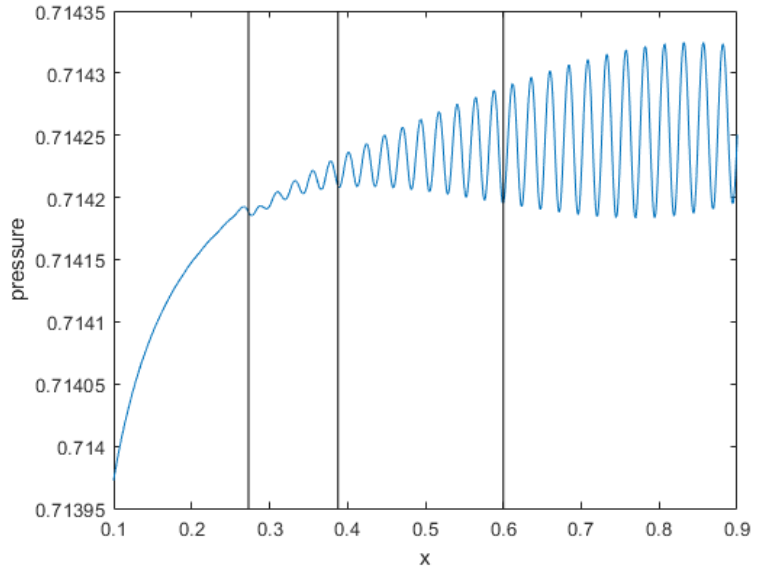

Figure 4.3 Evolution of x of pressure: excitation with no control.

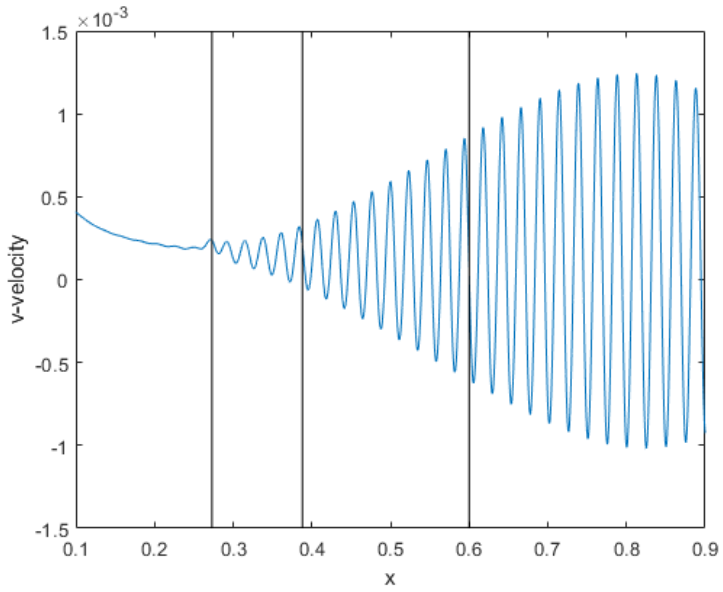

Figure 4.4 Evolution of x of v-velocity: excitation with no control.

4.2. Open-Loop Control

After TS instabilities are excited and are evident, the first level of control conducted is open-loop control to compare against Rizzetta and Visbal (2020). The non-dimensional amplitude of PDOS 2 for open-loop control is defined by a simple wave harmonic function, found in Equation 4.2.

$$amp = 4.4 \times 10^{-5} \sin(2\pi\omega\tau) + 1.34 \times 10^{-5} \cos(2\pi\omega\tau) \qquad [4.2]$$

Figure 4.5 below contains the contour plots of pressure (a) and v-velocity (b) for the open-loop control. Comparing these plots to those in Figure 4.1, suppression is visually observed. Continuously, Figure 4.5b can be compared against Figure 2.5b.

The actuation from PDOS 1 is active without PDOS 2 for 16τ (non-dimensional time). At this moment, PDOS 2 actuation is turned on. The time history plot of pressure for point O is shown in Figure 4.6. From the plot, suppression of the pressure oscillations

at point O is observed after 2τ from the moment PDOS 2 is turned on. Thus, the open-loop control successfully decreases instabilities.

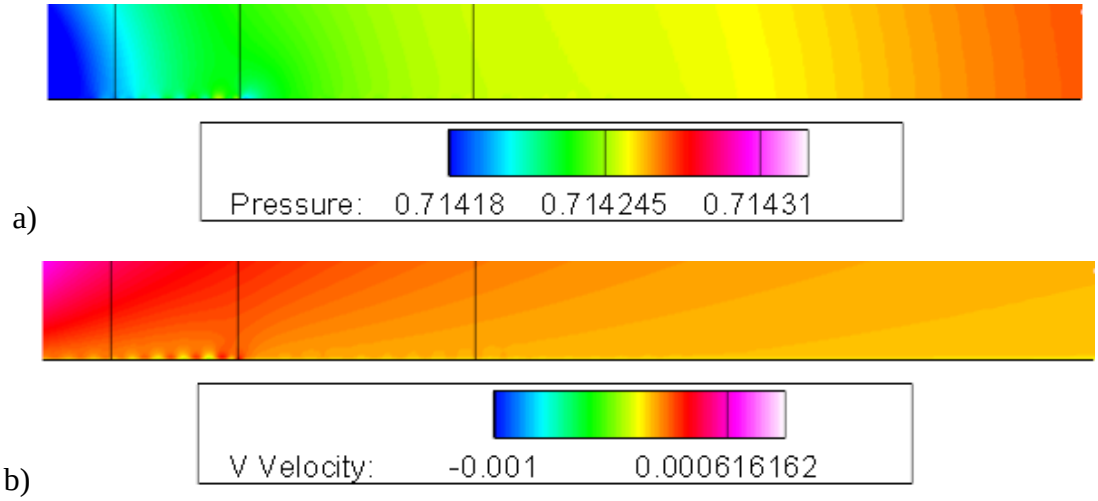

Figure 4.5 Actuation with open-loop control contour plots *a)* Pressure, *b)* V Velocity.

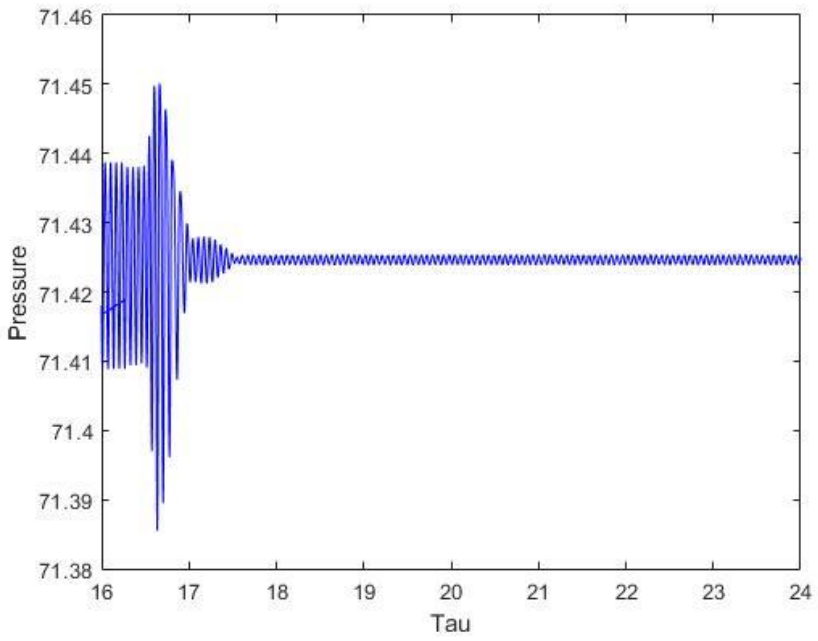

Figure 4.6 Time history plot at point O: excitation with open-loop control.

In Figures 4.7 and 4.8 the evolution of x of pressure and v-velocity are shown, respectively. They are plotted against results from Figures 4.3 and 4.4 when PDOS 2 is inactive. From the figures, suppression of the oscillations from PDOS 1 is evident downstream PDOS 2.

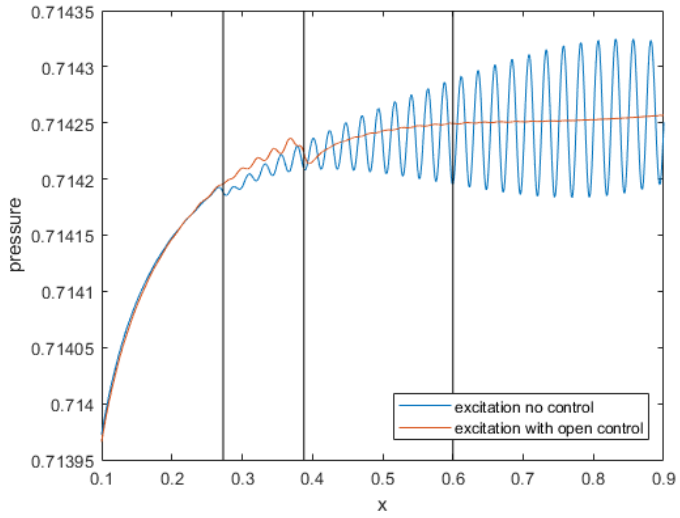

Figure 4.7 Evolution of x of pressure: excitation with open-loop control.

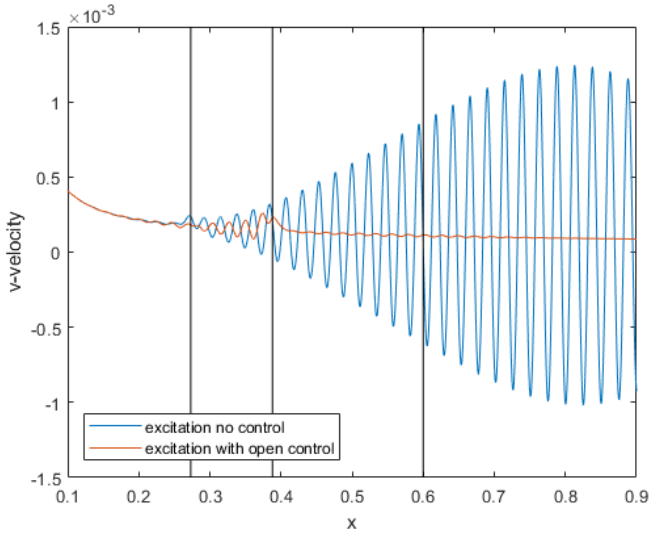

Figure 4.8 Evolution of x of v-velocity: excitation with open-loop control.

Figure 4.9 below shows the time-history of the actuator PDOS 2 amplitude from 15τ, 1τ before it is turned on. From the plot, the simple harmonics wave from Equation 4.2 is seen. This will be compared to the PDOS 2 amplitude for the closed-loop control tests.

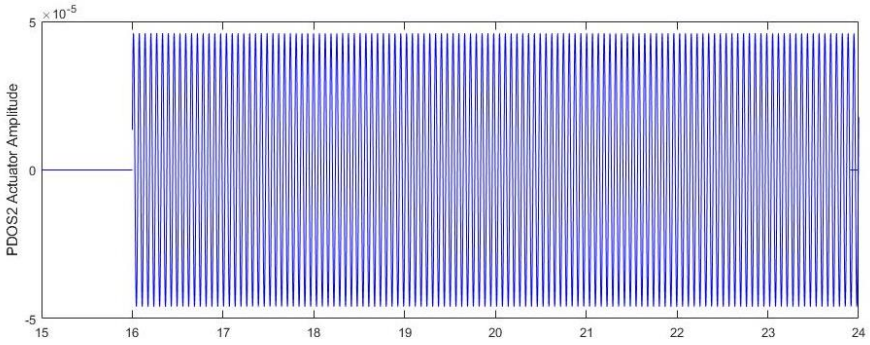

Figure 4.9 Open-Loop Control PDOS 2 Amplitude starting from 1 tau before actuation.

4.3. Closed-Loop Controller One

Closed-loop controller 1 is the simplified pressure-based controller designed by Dr. MacKunis of Embry-Riddle Aeronautical University's (ERAU) Physical Sciences Department. The controller uses input from a pressure sensor that is located downstream of PDOS 2. Different locations were tested for the pressure sensor.

4.3.1. Pressure Sensor Locations

The different sensor locations tested were x-locations S = 395 mm, 400 mm, and 500 mm from the leading edge. The first location was an initial test of CFD implementation of the sensor location and closed-loop controller. Later, the sensor was moved to 400 mm from the leading edge due to the practicality of actuator and sensor sizes for manufacturing purposes. Another sensor location test at 500 mm was also conducted for comparison against sensor location S=400mm.

4.3.1.1. Pressure Sensor Location 1: 395mm

The pressure sensor test with S = 395 mm from the leading edge was used to first test the implementation of the controller. This was done by analyzing the effect of perturbation pressure oscillations gathered by the sensor on the amplitude produced by PDOS 2. This comparison of amplitudes is shown in Figure 4.10. The value of F from Equation 3.12 is used to increase or decrease the amplitude of PDOS 2. Zooming in on Figure 4.10, we can see that the amplitude of PDOS 2 produced by the pressure-based closed-loop controller with a value of $F = 19^2$ is slightly larger than that of the open-loop amplitude of PDOS 2.

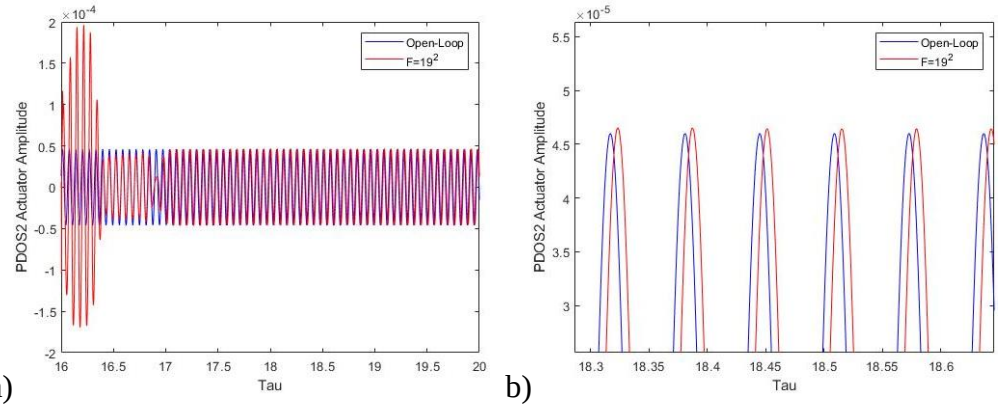

a) b)

Figure 4.10 a) PDOS 2 actuator amplitude time history plot, *b)* zoomed image of (a).

Furthermore, the perturbation pressure located at 600 mm was calculated and compared. Figure 4.11 shows the perturbation pressure comparison between open-loop control and closed-loop control with S = 395 mm. As seen in Figure 4.11a the perturbation pressure significantly decreases after the control is turned on at 16 tau. In Figure 4.11b, the perturbation pressure for the closed-loop control is slightly larger than that of the open-loop control. When comparing the perturbation pressures of the closed-

loop test from before and after control, there is roughly a 90% decrease in pressure perturbations. The contour plots of pressure and v-velocity for this pressure-based controller are below in Figure 4.12a and b respectively.

$$\frac{0.014 - .0013}{0.014} \times 100\% = 90.7\% \qquad [4.3]$$

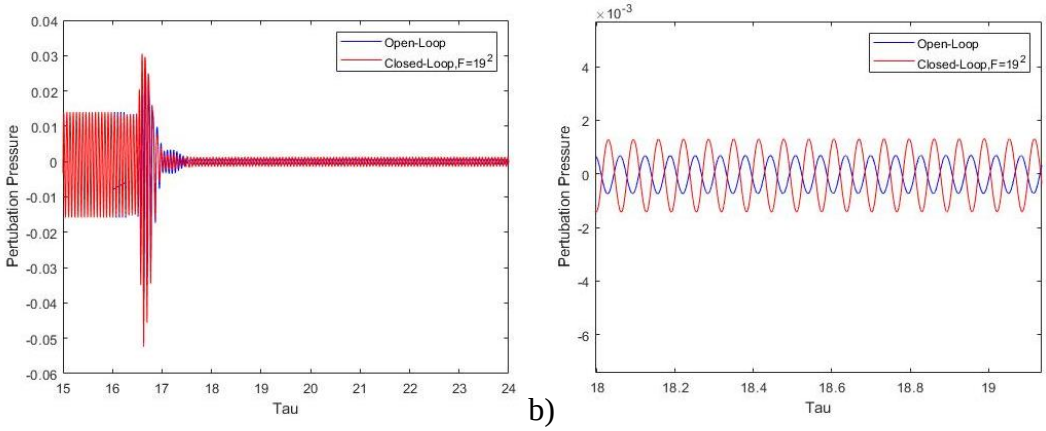

a) b)

Figure 4.11 a) Time history of perturbation pressure at x=600mm of open-loop control and closed-loop control when S=395mm, *b)* zoomed image of (a).

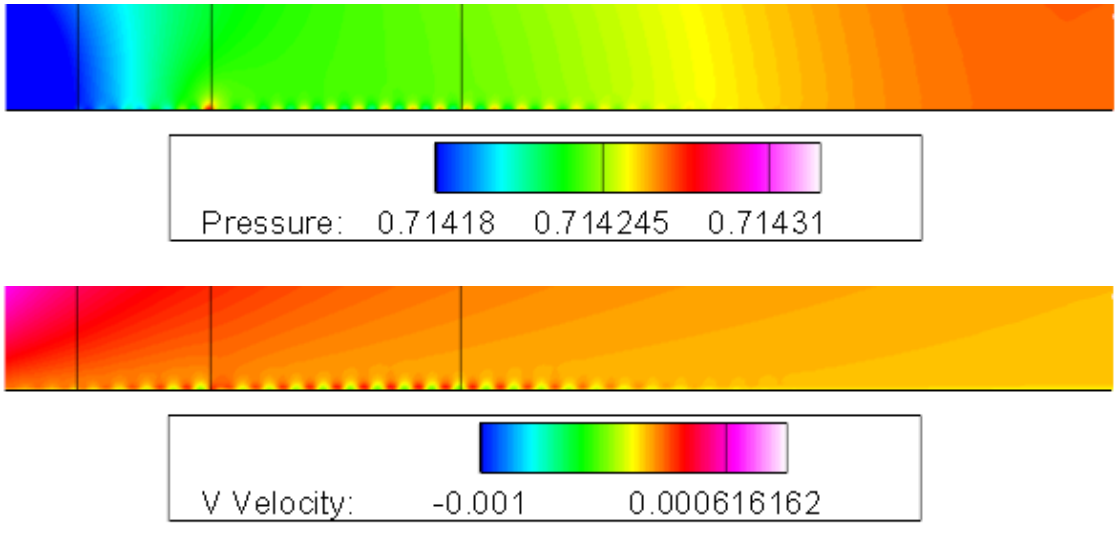

a)

b)

Figure 4.12 Actuation with closed-loop pressure controller when S=395mm contour plots a) Pressure, b) V Velocity.

4.3.1.2. Pressure Sensor Location 2: 400mm

The second sensor location tested is S=400mm. The same value of F = 19^2 is used. As seen from Figure 4.13, the amplitude and the phase shift of the PDOS 2 actuator amplitude changed due to the change in sensor location. A higher value of F is needed in order to achieve a closer relation to the PDOS 2 amplitude of open-loop control. However, when analyzing the pressure oscillations in Figure 4.14 we can see that even with a smaller amplitude, suppression is reached at point O.

Continuously, the pressure and v-velocity contour plots in Figure 4.15 show no significant changes when compared to Figure 4.12. This is expected, as S locations 395mm and 400mm are only 5mm apart. Though the amplitude has changed, the pressure perturbations have decreased significantly. When comparing the perturbation pressures of the closed-loop test from before and after control, there is roughly a 90% decrease in pressure perturbations.

$$\frac{0.014 - .0013}{0.014} \times 100\% = 90.7\% \qquad [4.4]$$

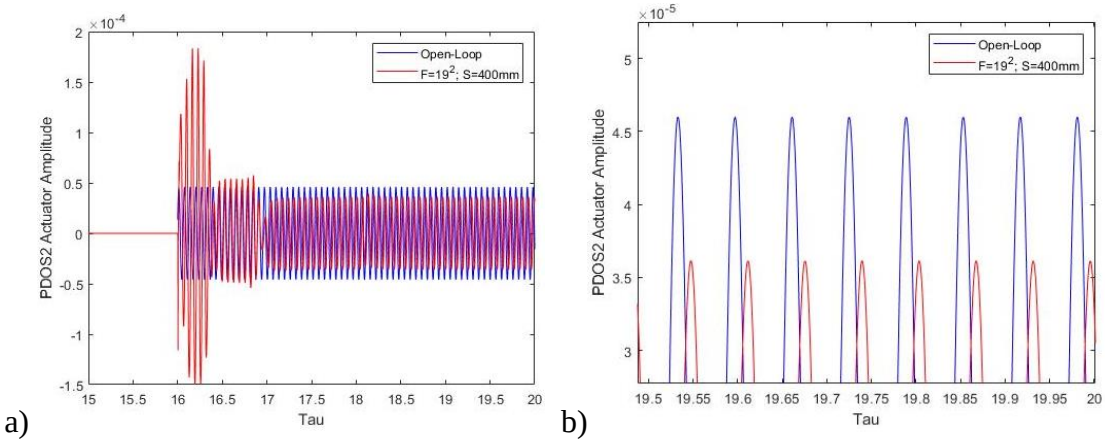

a) b)

Figure 4.13 a) PDOS 2 actuator amplitude time history plot, *b)* zoomed image of (a).

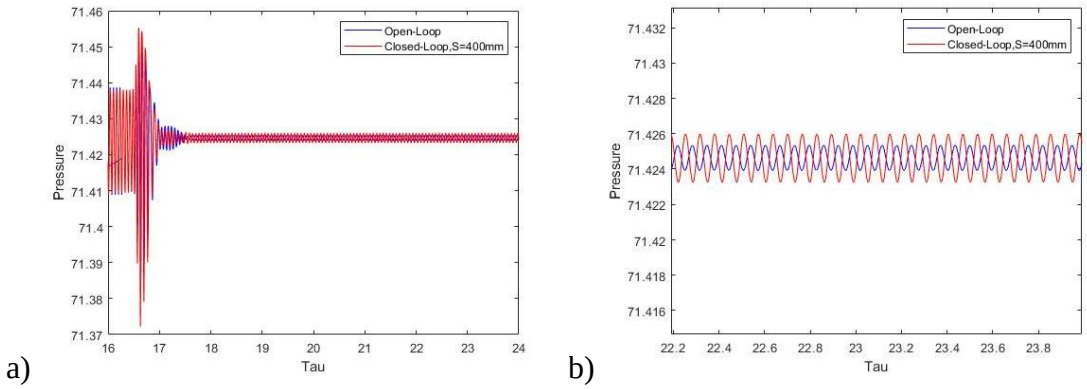

a) b)

Figure 4.14 a) Time history of pressure at x=600mm of open-loop control and closed-loop control when S=400mm, *b)* zoomed image of (a).

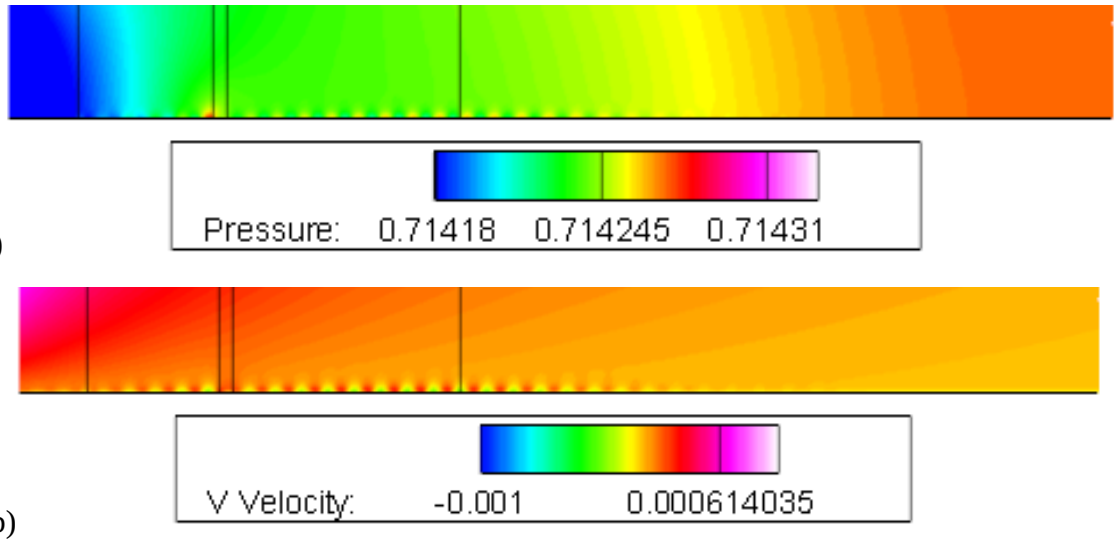

a)

b)

Figure 4.15 Actuation with closed-loop pressure controller when S=400mm contour plots a) Pressure, b) V Velocity. Vertical lines indicate locations from left to right: PDOS1, PDOS2, S, O.

When analyzing the evolution of x for pressure and v-velocity values oscillations are evident downstream of PDOS 2. The oscillations dampen out and are still significantly smaller than those in Figures 4.3 and 4.4. The comparison between open-loop and closed-loop controls are seen below in Figure 4.16 and 4.17. These plots show that suppression is achieved at a slower rate in comparison to open-loop control.

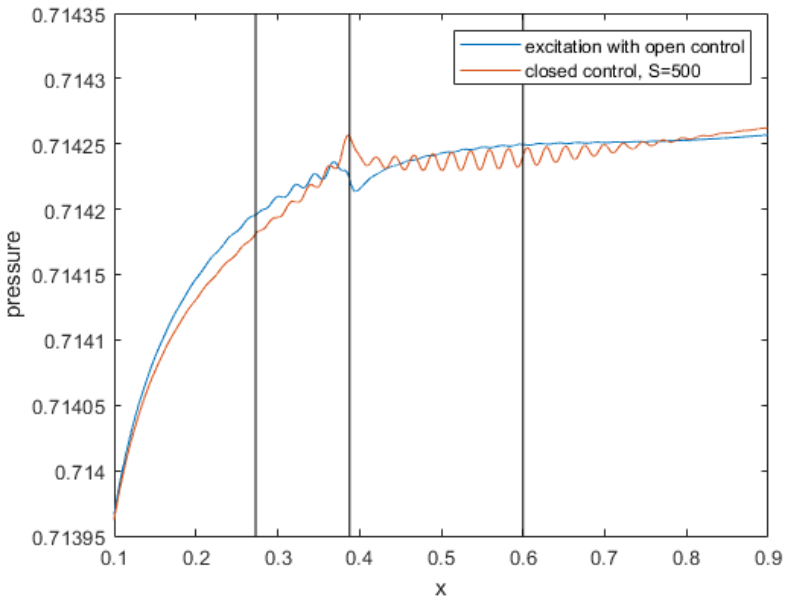

Figure 4.16 Evolution of x of pressure: open-loop control vs closed-loop control with S=400mm.

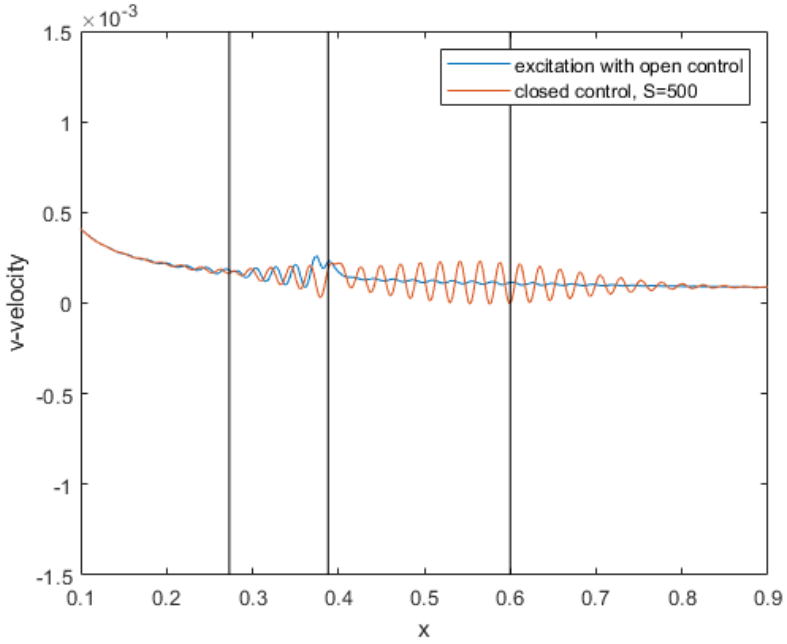

Figure 4.17 Evolution of x of v-velocity: open-loop control vs closed-loop control with S=400mm.

4.3.1.3. Pressure Sensor Location 2: 500mm

The third sensor location tested is S=500mm. Again, the same value of F = 19^2 is used. As seen from Figure 4.18, the amplitude and the phase shift of the PDOS 2 actuator amplitude has again changed due to the change in sensor location. It is observed that as the sensor location moves further downstream where higher TS instabilities are recorded, the phase shift of the PDOS 2 amplitude also changes.

When analyzing the pressure in Figure 4.19 we can still observe a decrease in amplitude. The pressure and v-velocity contour plots in Figure 4.20 also show no significant changes when compared to Figure 4.12 and Figure 4.15, thus there is a similar 90% decrease in pressure perturbations.

$$\frac{0.014 - .0013}{0.014} \times 100\% = 90.7\% \qquad [4.5]$$

When analyzing the evolution of x for pressure and v-velocity, the results were similar to that for S=400mm. The comparison between open-loop and closed-loop control for S=500mm are seen below in Figures 4.21 and 4.22. A comparison of the open loop and closed-loop results for S=400 and 500mm are discussed below in section 4.5.

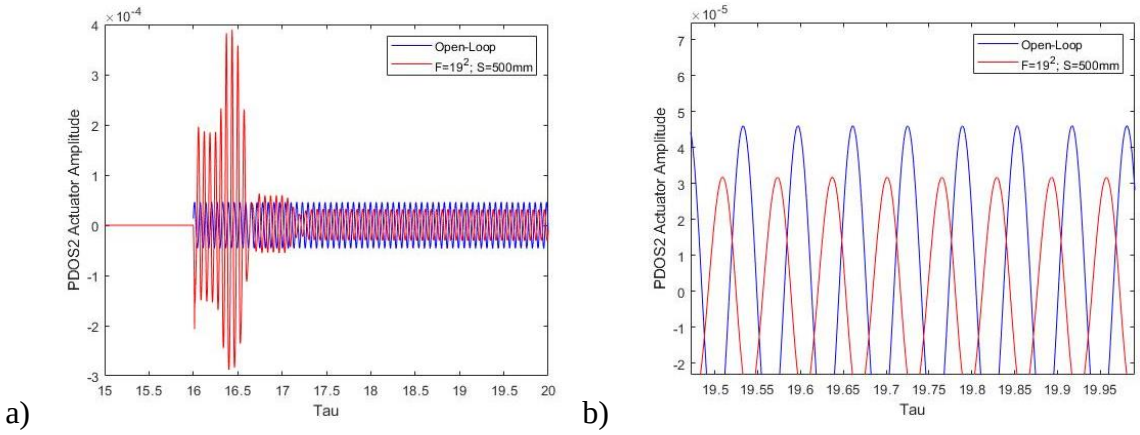

a) b)

Figure 4.18 a) PDOS 2 actuator amplitude time history plot, *b)* zoomed image of (a).

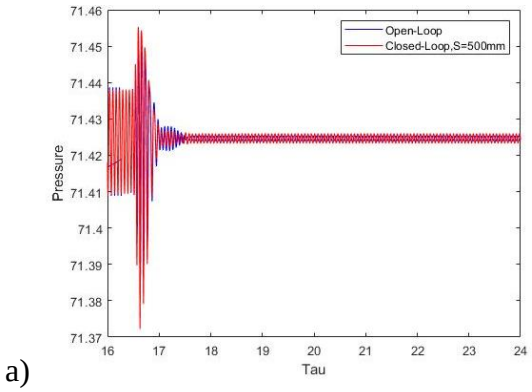

a)

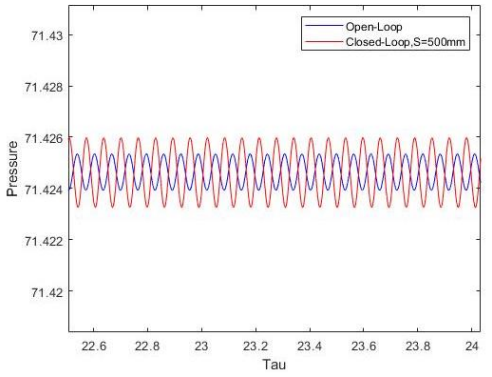

b)

Figure 4.19 a) Time history of perturbation pressure at x=600mm of open-loop control and closed-loop control when S=500mm, *b)* zoomed image of (a).

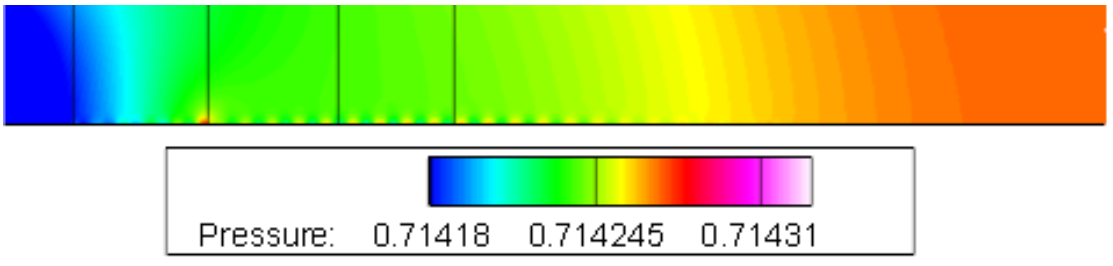

a)

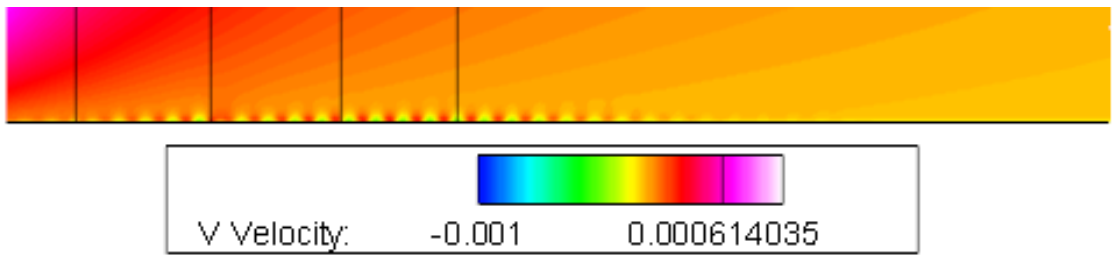

b)

Figure 4.20 Actuation with closed-loop pressure controller when S=500mm contour plots a) Pressure, b) V Velocity. Vertical lines indicate locations from left to right: PDOS1, PDOS2, S, O.

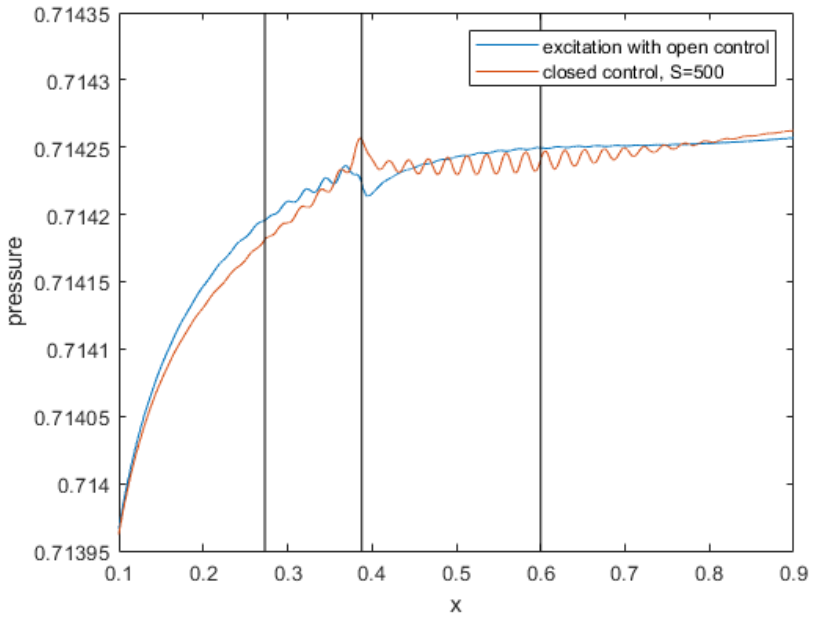

Figure 4.21 Evolution of x of pressure: open-loop control vs closed-loop control with S=500mm.

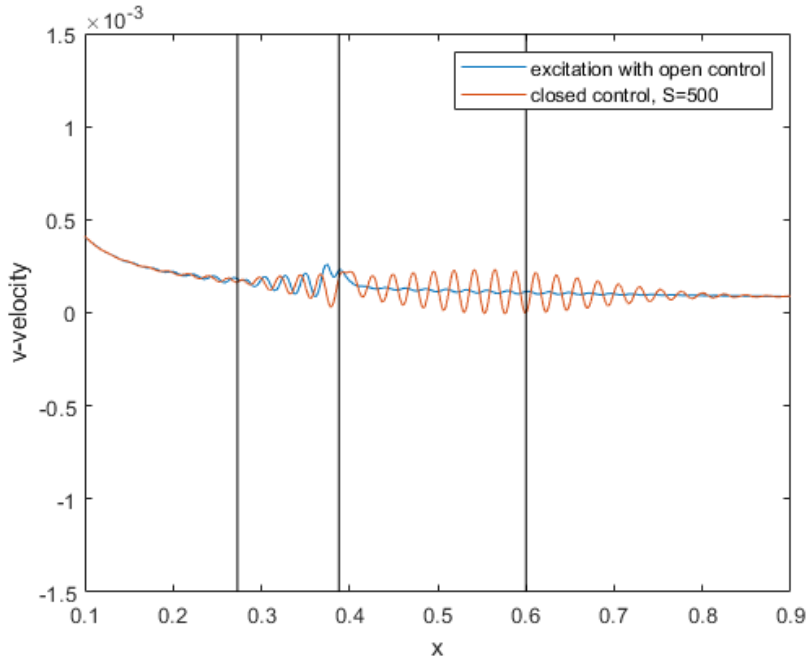

Figure 4.22 Evolution of x of v-velocity: open-loop control vs closed-loop control with S=500mm.

4.4. Closed-Loop Controller Two

Closed-loop controller 2 is the POD-ROM based controller. This controller first needs a POD analysis of the solution in order to generate the reduced order model. An initial spatial POD analysis was conducted using the entire CFD domain and 34 snapshots in time. This analysis was conducted on the excited cases with not control and open-loop control. Figure 4.23 below shows the pressure and v-velocity contour plots for the first three modes of the excitation with no control case.

Figure 4.24a shows a plot of the eigenvalues of the POD analysis with their corresponding mode. Figure 4.24b shows the plot of energy within the number of modes used for the excited and not control case. These plots show that the first 5 modes are critical in obtaining the most important flow characteristics for the excitation and no control case. Figures 4.25 and 4.26 are similar figures but for the excitation with open-loop case. Again, it is noted that the first 5 modes are the most critical. Table 4-1 contains the eigenvalues and energy values.

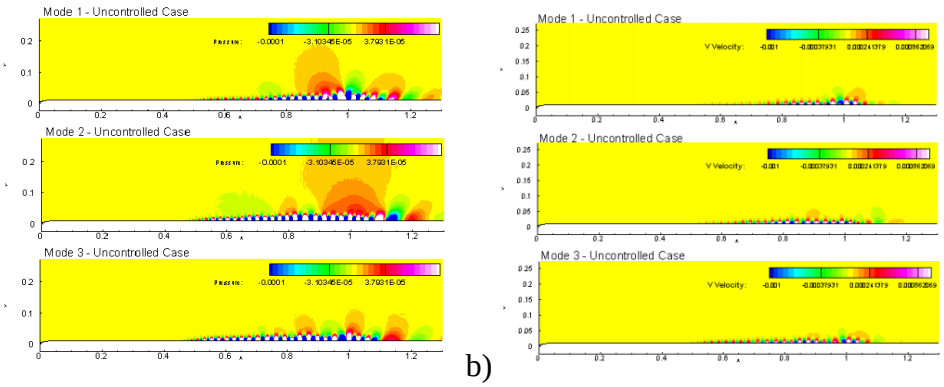

a) b)

Figure 4.23 First three modes (top to bottom) contour plots of the excitation and no control case, a) pressure (range from -1e-4 to 3.8e-5) and b) v-velocity (range from -1e-3 to 8.6e-3).

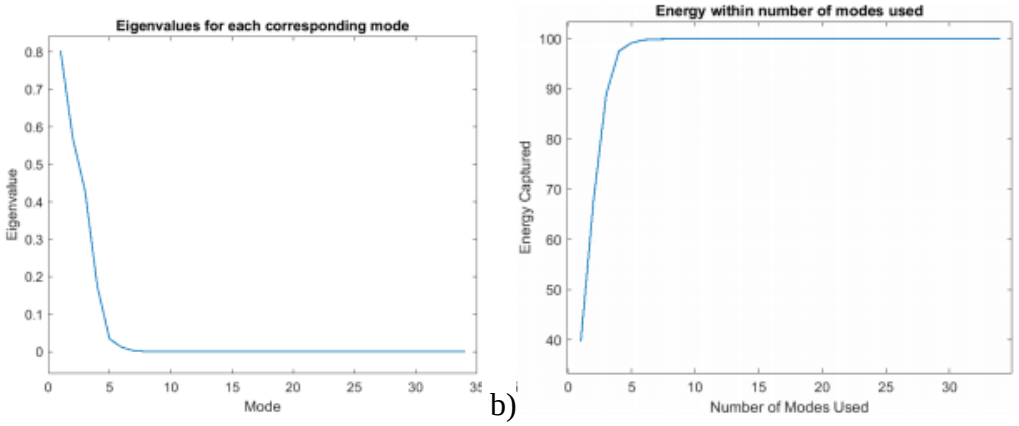

a) b)

Figure 4.24 a) Eigenvalues for each corresponding mode and b) Energy within number of modes used for the excitation with no control case.

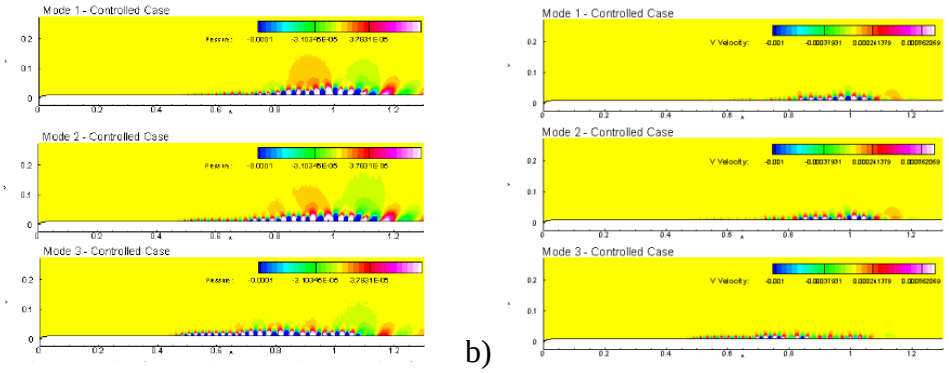

a) b)

Figure 4.25 First three modes (top to bottom) contour plots of the excitation and open-loop control case, a) pressure (range from -1e-4 to 3.8e-5) and b) v-velocity (range from -1e-3 to 8.6e-3).

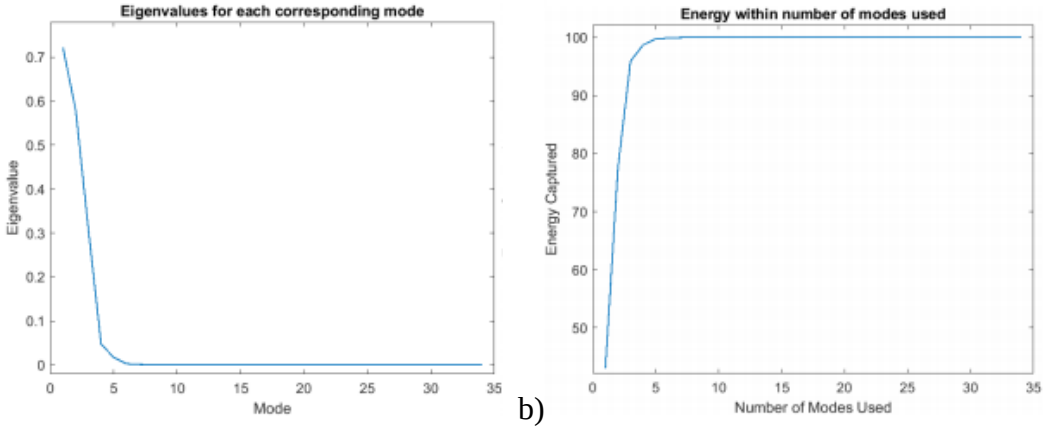

a) b)

Figure 4.26 a) Eigenvalues for each corresponding mode and b) Energy within number of modes used for the excitation with open-loop control case.

Table 4.1 Eigenvalue and energy values with r modes.

	Uncontrolled Case		**Open-Loop Controlled Case**	
r	**Eigenvalues**	**Energy Captured with r modes**	**Eigenvalues**	**Energy Captured with r modes**
1	0.8032	39.63682	0.7209	43.01226
2	0.5695	67.74045	0.5787	77.54342
3	0.4295	88.93734	0.3075	95.89220
4	0.1741	97.52911	0.0469	98.69166
5	0.0341	99.21176	0.0174	99.72690
6	0.0117	99.78946	0.0028	99.89143
7	0.0026	99.91845	0.0011	99.95487
8	0.00077	99.95650	0.00043	99.98068
9	0.00032	99.97239	0.00017	99.99091
10	0.00026	99.98529	0.000078	99.99555

With 5 modes obtaining 99% of the energy captured within the flow, Equation 3.18 becomes the following,

$$y = c_1x_1 + c_2x_2 + c_3x_3 + c_4x_4 + c_5x_5 \quad [4.6]$$

If considering only one mode, the equation simplifies to Equation 4.7 below.

$$y = c_1x_1 \quad [4.7]$$

Comparing Equation 4.7 with one mode to Equation 3.10 from the pressure-based controller, one could say that the pressure-based controller approximates a POD-ROM controller utilizing one mode.

4.5. Comparison of Results

The contour plots side-by-side for easy comparison is found in Appendix A. Figures 4.27 and 4.28 are the evolution of x for pressure and v-velocity values for the open-loop case, closed-loop cases S=400mm and 500mm, and the uncontrolled case. From these plots, it is evident that the suppression rate of closed-loop cases S=400mm and S=500mm contain very little to no difference.

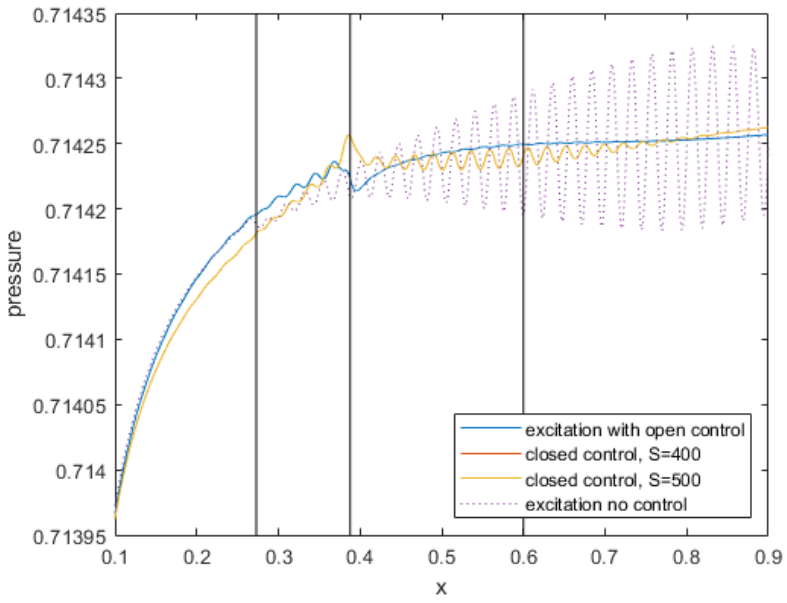

Figure 4.27 Evolution of x of pressure for open control, closed-loop controls for S=400mm and 500mm, and no control.

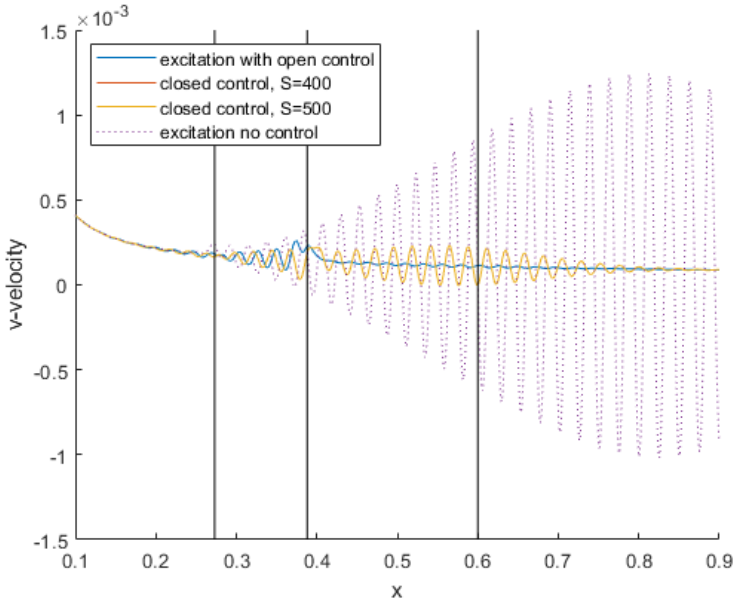

Figure 4.28 Evolution of x of v-velocity for open control, closed-loop controls for S=400mm and 500mm, and no control.

5. Discussions, Conclusions, and Recommendations

The flat plate model with excited TS waves and open-loop control was successfully recreated to allow further comparisons with closed-loop control. The pressure-based controller was successfully developed, implemented and suppressed TS fluctuations. The POD-ROM is still under development and is unclear if suppression will be more effective with multiple modes. At the outset, this project presents a further understanding in transitional control, resulting in a significant reduction of instabilities produced on a flat plate.

5.1. Conclusions

The results presented in this work is highly dependent on three important factors, which are: 1) the excited TS instabilities produced by PDOS 1; 2) control laws; and 3) geometry. Due to the delicacy of natural transition, a change in any of these parameters could prove to be beneficial or detrimental to successful transitional control.

Transitional control on a flat plate was successfully simulated on FDL3DI. This work serves to be a virtual representation using closed-loop controller designs and serves as a benchmark for the optimal transitional control on real airfoil geometry. After testing a variety of scenarios in the simulation environment, the most significant results from this work are listed below:

- Results indicate that the Pressure-Based Closed-Loop Controller was able to suppress TS instabilities observed in pressure perturbations by 90%.
- When compared to the simple open-loop controller, there is a 50% increase in pressure perturbations, concluding that open-loop control is more successful in suppressing 2-D TS waves.

- Though suppression is achieved with the pressure based closed-loop controller, the open-loop controller suppresses the TS waves much quicker.
- The sensor locations S=400mm and S=500mm provided very similar outcomes at the observer point O.
- Mathematically speaking, the pressure-based controller can serve as an approximation of the POD-ROM controller with one mode.

These results provide the hopeful indication on the possibilities of implementing PDOS actuators employed by a pressure-based controller for suppressing 2-D TS instabilities. This is a rudimentary proof of concept that shows the feasibility of transition control with a closed-loop controller on a flat plate. In addition to this, the prospect of this controller can be implemented and tested on real airfoil geometry.

5.2. Recommendations

While the open-loop system is clearly superior to the pressure-based closed-loop system, it was also observed that different freestream conditions and airfoil geometry could significantly alter the results. This comparison would provide the rationale for the need to develop a nonlinear control system that can minimize any instabilities produced in the boundary layer.

As the scenarios described above are discussed, the need for implementing artificial intelligence transition control was realized. More specifically, it was determined that a POD-ROM closed-loop controller has the potential for the best methodology for this study. This ROM paradigm would establish the rationale for optimal transitional control under any environmental conditions. This leads to the next important step in this research, where a POD-ROM controller tested on different airfoil geometries and

environmental conditions could be fabricated and a deeper understanding of transitional control would be achieved.

REFERENCES

Amitay, M., Tuna, B.A., & Dell'Orso, H. (2016). Identification and Mitigation of T-S Waves using localized Dynamic Surface Modification. *Physics of Fluids, 28*(6). https://doi.org/10.1063/1.4953844

Anderson, J. (2017). *Fundamentals of Aerodynamics Sixth Edition*. New York, NY: McGraw-Hill Education.

US Air Force Research Lab. (1998). *High-Order Schemes for Navier-Stokes Equations: Algorithm and Implementation into FDL3DI* (ADA364301). Wright-Patterson AFB, OH: Air Force Research Laboratory.

Guay, M., & Hariharan, N. (2008). Airflow velocity estimation in Building Systems. *2008 American Control Conference*, 908-913. Seattle, WA. doi: 10.1109/ACC.2008.4586608

Kidambi, K.B., MacKunis, W., & Jayaprakash, A.K. (2020). Limit Cycle Oscillation Suppression Using a Closed-loop Nonlinear Active Flow Control Technique. *2020 59th IEEE Conference on Decision and Control (CDC)*, 5507-5512. Jeju, Korea. doi: 10.1109/CDC42340.2020.9303839.

Kotsonis, M., Giepman, R., Hulshoff, S., & Veldhuis, L. (2013). Numerical study of the Control of Tollmien-Schlichting Waves Using Plasma Actuators. *AIAA Journal, 51*(10). doi: 10.2514/1.J051766

Rizzetta, D. P., & Visbal, M.R. (2020). Closed-Loop Control of Transition by Local Dynamic Surface Modification. *AIAA SciTech 2020 Forum*. https://doi.org/10.2514/6.2020-0096

Rizzetta, D. P., & Visbal, M.R. (2019). Direct Numerical Simulation of Transitional Control via Local Dynamic Surface Modification. *AIAA Journal, 57*(8), https://doi.org/10.2514/1.J057664

Rizzetta, D. P., & Visbal, M.R. (2019). Investigation of Transition Delay by Dynamic Surface Deformation. *ASME Journal of Fluids Engineering, 141*(12). https://doi.org/10.1115/1.4043859

Sirovich, L. (1987). Turbulence and the Dynamics of Coherent Structures Part III: Dynamics and Scaling. *Quarterly of Applied Mathematics, 45*(3), 583-590. doi: 10.1090/qam/910464

Taira, K., Brunton, S.L., Dawson, S.T.M., Roawley, C.W., et al. (2017). Modal Analysis of Fluid Flows: An Overview. *AIAA Fluid Dynamics, 55*(12). https://doi.org/10.2514/1.J056060

White, F. M. (2006). *Viscous Fluid Flow Third Edition*. New York, NY: McGraw Hill Education.

Appendix A

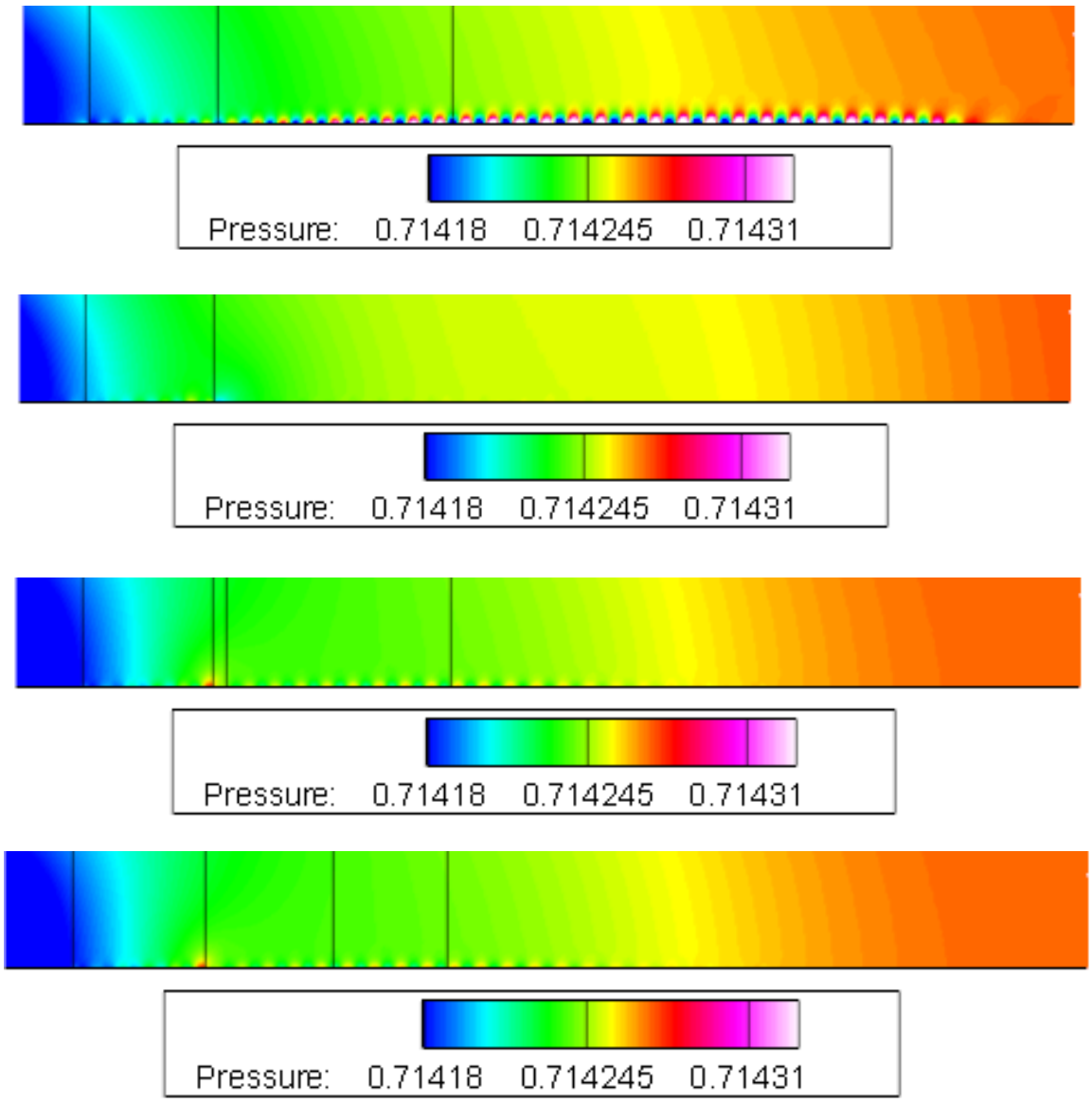

Figure A.1 Pressure Contour Plots for top to bottom: excitation with no control, excitation with open-loop control, excitation with closed-loop control and S=400mm, and excitation with closed-loop control and S=500mm.

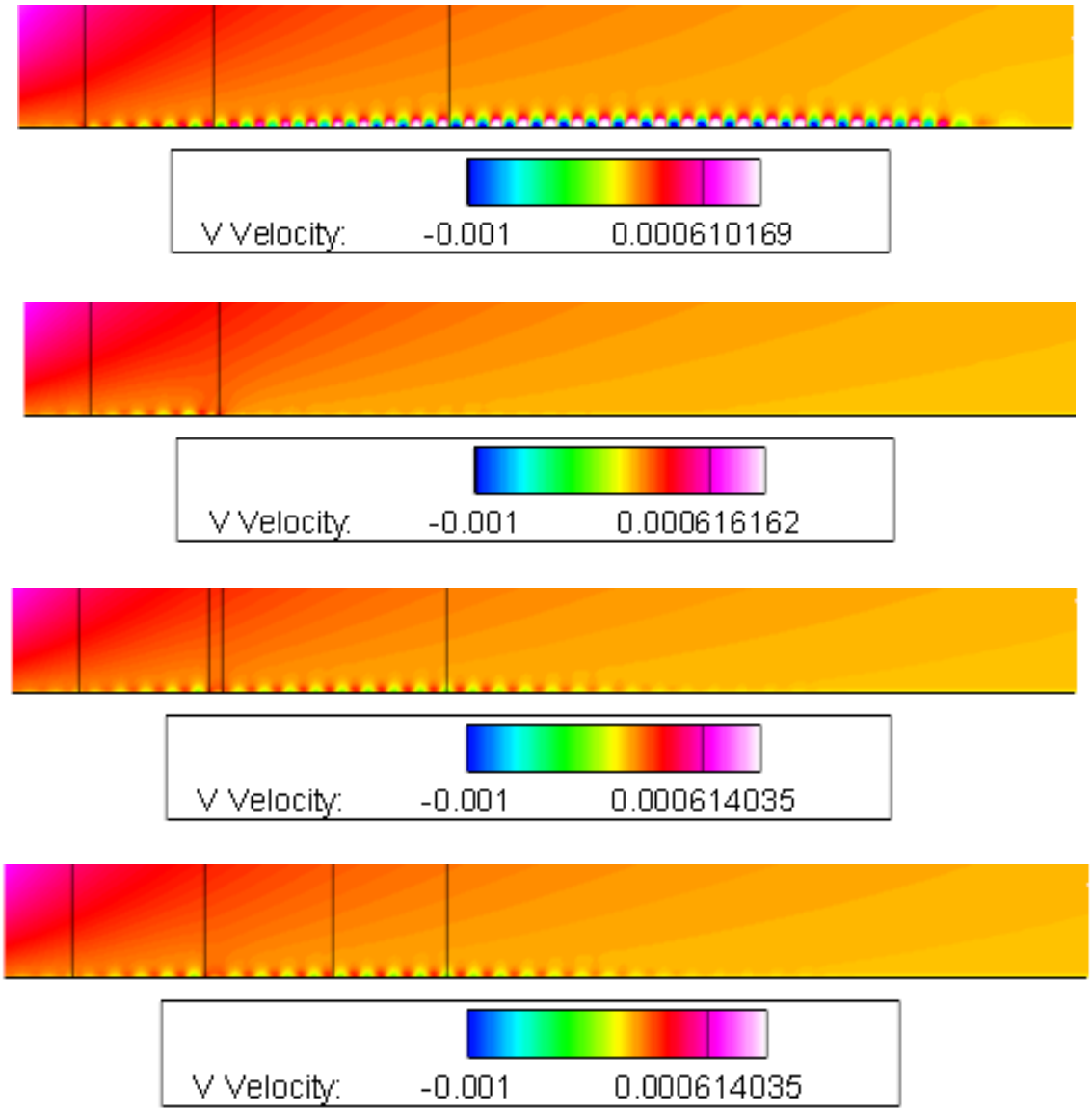

Figure A.2 V Velocity Contour Plots for top to bottom: excitation with no control, excitation with open-loop control, excitation with closed-loop control and S=400mm, and excitation with closed-loop control and S=500mm.